

Chapter 6

Microwave Sensors – Active and Passive

David G. Long

Electrical and Computer Engineering Department
Brigham Young University Center for Remote Sensing
459 Clyde Building, Provo, UT 84602, long@ee.byu.edu

Revision Date: January 28, 2008

Summary

Microwave remote sensing instruments provide another view of the environment which can augment traditional visible and infrared observations. Microwave sensors can be classified as either passive (radiometers) or active (radars). Each sensor class provides unique insight into the electrical and mechanical properties of the sensed environment. This chapter provides a very brief overview of microwave remote sensing along with summaries of the capabilities of major microwave sensors, particularly space-based sensors.

6.1 Introduction

The electromagnetic spectrum extends from low frequency radio waves up through high energy gamma waves. Microwaves extend over an important part of the electromagnetic spectrum. Typically microwaves are defined as frequencies from approximately 1 GHz to 300 GHz (Fig. 6.1), corresponding to an electromagnetic

wavelength range of 1 m to 1 mm (Ulaby et al., 1981). At the low end of this range, the Earth's atmosphere is transparent, but becomes more opaque with increasing frequencies. Over the range of microwave frequencies, the radiative emission and absorption of the atmosphere is sensitive to geophysical parameters such as moisture, rainfall, and temperature. Thus, microwaves play an important role in remote sensing of the atmosphere as well as the Earth's surface. Microwaves are also widely used in astronomy to study cosmic phenomena.

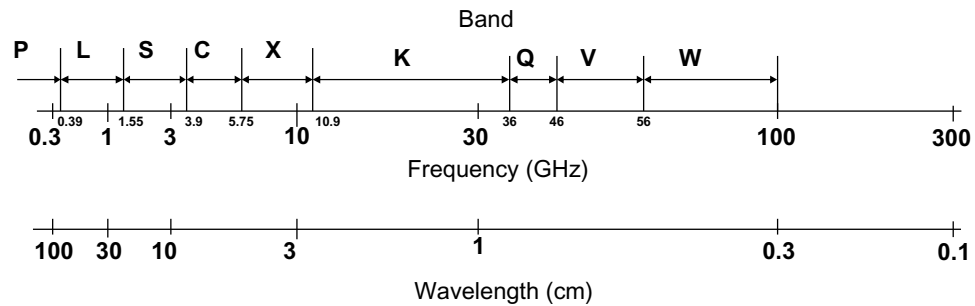


Figure 6.1: Illustration of the microwave region of the electromagnetic spectrum with common band definitions shown. The precise band definitions vary among authors.

Microwave sensors have been flown on aircraft and spacecraft and have become standard instruments for operational observations of the Earth. Extensive databases of observations made by various types of sensors at different frequencies have been collected of the Earth, the outer planets, and beyond. This chapter briefly considers the theory and methods of microwave remote sensing. While the focus is on airborne and spaceborne observations of the Earth, other sensors and targets are considered. The primary goal of this chapter is to provide some sensor-specific information on past, present, and future microwave sensors and summarize a few key analysis techniques and applications. Major sensors and/or sensor technologies are briefly described, though only non-military sensors which have provided data sets available to the general remote sensing community are included.

After this introduction, the next section focuses on passive microwave sensors. The succeeding section discusses radar systems. In each section the general theory of operation of the sensor class is provided, followed by a very brief description of selected sensors. Further information is available in the cited literature. A general introduction to microwave remote sensing concludes this section.

6.1.1 Passive versus active microwave sensing

Microwave remote sensing instruments can be divided into two broad classes: passive, known as radiometers, and active, known as radars, see Fig. 6.2 (Skou and Le Vine, 2006; Ulaby et al., 1981; Woodhouse, 2006). The latter from radiometers in that they include a transmitter. Both classes of sensors have been used on aircraft and spacecraft to study the Earth and the other planets.

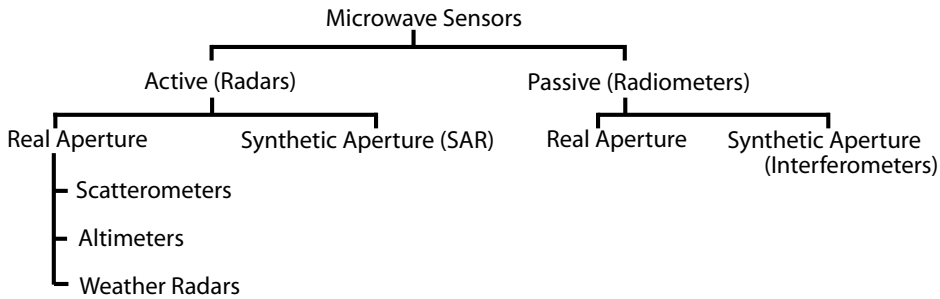


Figure 6.2: Organization of the major classes of microwave remote sensors.

Active microwave sensors can be further divided into four general classes: synthetic aperture radar (SAR) systems, scatterometers, altimeters, and weather radars. The latter systems typically use real-aperture antennas while SAR is based on synthetic aperture antenna processing techniques. Some hybrid systems have been developed. Inverse synthetic aperture radar has been used for ground-based sensing of extra-terrestrial bodies.

SAR systems are radars designed to make high resolution radar images. They operate by transmitting modulated pulses and using Doppler/range processing to construct backscatter images. Typically, they are not as well calibrated as scatterometers. Scatterometers are designed to measure radar backscatter very precisely, but typically have lower resolution than SARs. They tend to be less complicated than SARs. Altimeters are radars designed to measure height or distance, though other information such as radar backscatter is extracted from the echo. Weather radars are specially designed scatterometers which have ranging capability. They are designed to measure rainfall and other meteorological phenomena.

Passive microwave sensors rely on the thermal emission of microwave signals from objects. The emission is related to the physical temperature and electrical properties of the sensed surface (Fung, 1994), with modulation by the intervening atmosphere (Ulaby et al., 1981). Since they contain no transmitter, passive sensors typically require less power to operate. To reduce the noise level of the measure-

ments they typically operate over a broader frequency range (band) than do radar sensors, which tend to be narrow band. While most radiometers use real-aperture antennas, radiometer-interferometers often rely on multiple antennas (Goodberlet, 2000; Ruf et al., 1988; Wohlleben et al., 1991).

6.1.2 Airborne Versus Spaceborne Sensing

The first microwave sensors were ground-based, but aircraft-based applications quickly followed. Microwave radar systems were first deployed on aircraft in World War II and microwave sensors flew aboard spacecraft early in the space age. Ground-based microwave sensors have been widely used in astronomy and weather.

Currently, some of the most important Earth sensing microwave instruments are based on spacecraft. Spacecraft basing offers a number of advantages over aircraft-basing, including much broader spatial (often global) and temporal coverage. However, operational costs are much higher for orbiting sensors than flying them on aircraft. Government agencies such as the U.S. National Oceanic and Atmospheric Administration (NOAA), the U.S. National Aeronautics and Space Administration (NASA), the Russian Space Agency (RKA), the European Space Agency (ESA), and the Japan Aerospace Exploration Agency (JAXA) operate a fleet of spacecraft carrying a variety of microwave sensors. The Indian and Chinese governments are also rapidly developing spaceborne microwave sensors. Data from past and present sensors have been archived and are readily available to researchers.

6.1.2.1 Spaceborne Microwave Sensors

A variety of active and passive microwave remote sensing instruments have flown in space. The landmark Seasat-1 mission was probably the most important early spacecraft-based microwave remote sensing missions (Barrick and Swift, 1980; Born et al., 1979). It flew in 1978 and carried a microwave radiometer, an altimeter, a scatterometer, and a SAR. The Seasat-1 mission clearly demonstrated the utility of these sensors, and led to multiple follow-on missions.

Some of the most important of these have collected long time series. These include include the Special Sensor Microwave Radiometer (SMMR) first flown aboard NIMBUS and Seasat-1 in 1978; the Special Sensor Microwave Imager (SSM/I) radiometer (Hollinger et al., 1990, 1987), continuously flown on Defense Meteorological Satellite Program (DMSP) spacecraft since the early 1980's; the Earth Resources Satellite (ERS-1/2) Active Microwave Instrument (AMI) (Attema, 1991), which operated from 1982 through 2001 in scatterometer and SAR modes; the SeaWinds instrument (Spencer et al., 2000) which has operated aboard

QuikSCAT since 1999; the Advanced Microwave Sensor Radiometer (AMSR) operating on several spacecraft; the precipitation radar and radiometer aboard the Tropical Rain Mapping Mission (TRMM) satellite; the polarimetric WindSat radiometer, and a series of ocean altimeters that began with Topex/Poseidon.

A number of synthetic aperture radar (SAR) systems have flown in space including a SAR aboard Seasat in 1978, the Shuttle Imaging Radar (SIR) series (SIR-A, SIR-B, SIR-C/X-SAR, and SRTM), ERS-1/2, Radarsat-1, and Envisat. Altimeter missions include the Seasat altimeter, the landmark Topex/Poseidon altimeter mission that operated from 1989-2005, the ERS-1/2 altimeters, and Jason-1/2. Together these instruments have demonstrated the utility of microwave sensors in the study and monitoring of the Earth's land, ocean, and atmosphere.

For space-based Earth sensing, SAR systems are generally very high resolution (often 100 m and finer) but low coverage while spaceborne radiometers and scatterometers have lower resolution sensors (12 to 75 km) but broader coverage. The resolution of these low resolution sensors is suitable for the oceanic and atmospheric applications for which they were designed, but there is growing interest in applying such microwave sensor data in new applications requiring higher resolution.

Scatterometers operate by transmitting a pulse of microwave energy towards the Earth's surface and measuring the reflected energy. The backscattered energy is related to the normalized radar cross-section (σ^o) via the radar equation (Ulaby et al., 1981). The spatial response function of the sensor determines the spatial resolution of the σ^o observation, with typical resolutions varying from 25 to 50 km. Originally designed for retrieval of near-surface winds over the ocean (indirectly via measurements of the Bragg scattering from the wind-generated wave field of the surface (Naderi et al., 1991; Ulaby et al., 1981; Elachi and van Zyl, 2006)), scatterometer data is now being applied to the study of tropical vegetation, polar ice, and global change, e.g. (Ashcraft and Long, 2004; Attema et al., 1998; Forster et al., 2001; Lecomte et al., 1993; Long and Drinkwater, 1999; Long et al., 2001; Remund and Long, 1999; Wisman et al., 1995). Scatterometer data is also being operationally used in weather forecasting and sea-ice monitoring (Ashcraft and Long, 2004).

Radiometers are passive, receive-only sensors which measure the thermal emission (brightness temperature) of the target in the microwave band (Fung, 1994; Tsang et al., 1985; Ulaby et al., 1981; Woodhouse, 2006). The apparent scene brightness temperature is related to the emissivity and temperature of the surface and is modified by moisture content (Kraszewski, 1996) and temperature of the intervening atmosphere. By appropriate selection of operating frequencies in several microwave bands, the temperature and moisture content of the atmosphere (Jones and Haar, 1990), as well as key surface properties such as land surface tem-

perature (McFarland et al., 1990), soil and plant moisture (Jackson and Schmugge, 1989; Pampaloni and Paloscia, 1986), sea-ice mapping (Thomas et al., 1985), snow cover classification (Grody et al., 1991), and wind speed (over the ocean) (Wentz, 1991), can be retrieved. Radiometer data is being operationally used in weather forecasting and sea-ice monitoring. Radiometers are also used for correcting path length variations in altimetry (Bernard et al., 1993; Fu et al., 1994; Ruf et al., 1995). Ground-based radiometers are used for measuring meteorological variables (Janssen, 1993) and radio astronomy (Burke and Graham-Smith, 2002; Verschuur et al., 1987; Rohlfis and Wilson, 1996). Microwave limb sounders are specialized radiometers which measure vertical profiles of atmospheric brightness temperature by looking horizontally through the atmosphere. From this data, vertical profiles of temperature, pressure and moisture can be extracted. Limb sounders are not treated in this chapter.

Altimeters are ranging radars designed to measure the distance from a spacecraft or aircraft to the ground. With a carefully measured spacecraft orbit, height accuracies to a few cm are possible (Fu et al., 1994). From the altimeter height measurements, surface topography can be measured. Over the ocean the surface topography can be related to ocean currents and undersea topography. Other information such as ocean wave height and near-surface wind speed can also be extracted. Altimeter data has also been used for creating digital elevation maps of polar regions, e.g., (Bamber, 1994; Zwally et al., 1983).

Weather radars are ranging scatterometers designed to measure rainfall (Doviak et al., 1979; Doviak and Zrnicek, 1984; Meneghini and Kozu, 1990). Some weather radars can measure radial velocity and thus can determine wind as well as rain. Ground-based weather radars (i.e., NEXRAD) have been extensively deployed and data from them are often displayed on television news and weather broadcasts. To-date, the only space-based orbital weather radars have been the Tropical Rain Mapping Mission (TRMM) Precipitation Radar (PR) and Cloudsat. TRMM also carried a radiometer, the TRMM Microwave Imager (TMI) (Awaka et al., 1997; Meneghini et al., 2000).

6.2 Passive Systems (Radiometers)

6.2.1 Background

Microwave radiometers measure the thermal emission, sometimes called the Planck radiation, radiating from natural objects (Ulaby et al., 1981; Woodhouse, 2006). As passive sensors they require no transmitter but are receive-only. As a result, radiometers require less power to operate than radars.

6.2.1.1 Radiometer Fundamentals

In a typical radiometer, an antenna is scanned over the scene of interest and the output power from the carefully calibrated receiver is measured as a function of scan position. The observed power is related to the receiver gain and noise figure, the antenna loss, the physical temperature of the antenna, the antenna pattern, and the scene brightness temperature. In simplified form, the output power P_{SYS} of the receiver can be written,

$$P_{\text{SYS}} = kT_{\text{SYS}}B \quad (6.1)$$

where $k = 1.38 \times 10^{-28}$ is Boltzmann's constant, B is the receiver bandwidth and T_{SYS} is the system temperature,

$$T_{\text{SYS}} = \eta_l T_A + (1 - \eta_l) T_p + (L - 1) T_p + L T_{\text{REC}} \quad (6.2)$$

where η_l is the antenna loss efficiency, T_p is the physical temperature of the antenna and waveguide feed, L is waveguide loss, T_{REC} is the effective receiver noise temperature (determined by system calibration), and T_A is the effective antenna temperature. The effective antenna temperature is dependent on the direction the antenna points and the scene characteristics.

The effective antenna temperature, T_A can be modeled as a product of the apparent temperature distribution $T_{AP}(\theta, \phi)$ in the look direction θ, ϕ (see Fig. 6.3) the antenna radiation gain $F(\theta, \phi)$ which is proportional to the antenna gain pattern $G(\theta, \phi)$.

T_A (in K) is obtained by integrating the product of apparent temperature distribution $T_{AP}(\theta, \phi)$ (in K) at the antenna pattern $G(\theta, \phi)$:

$$T_A = \frac{1}{\bar{G}} \iint G(\theta, \phi) T_{AP}(\theta, \phi) d\theta d\phi \quad (6.3)$$

where

$$\bar{G} = \iint G(\theta, \phi) d\theta d\phi \quad (6.4)$$

where integrals are over the range of values corresponding to the non-negligible gain of the antenna. Note that the antenna pattern acts as a low pass filter of the surface brightness, limiting the effective spatial resolution of the measurement to approximately the 3 dB beamwidth. The observed value can be split into contributions from the mainlobe and the sidelobes,

$$T_a = \eta_M \bar{T}_{ML} + (1 - \eta_M) \bar{T}_{SL} \quad (6.5)$$

where η_M is the main lobe efficiency factor

$$\eta_M = \frac{1}{\bar{G}} \iint_{\text{main lobe}} G_i(\theta, \phi) d\theta d\phi \quad (6.6)$$

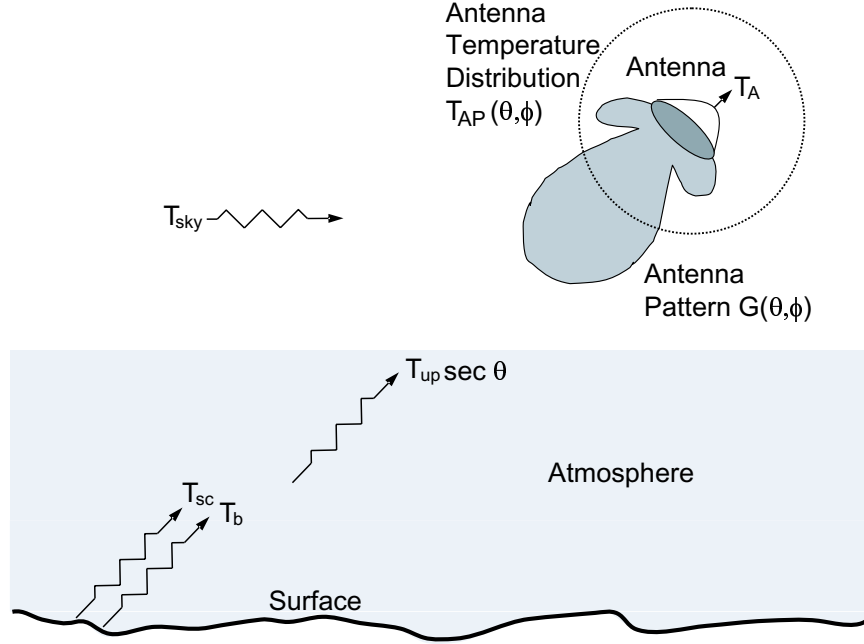


Figure 6.3: The apparent temperature distribution and some of its contributions. The antenna temperature T_A is the normalized integral of product of the temperature distribution and the antenna gain pattern. The apparent temperature of the surface seen through the atmosphere includes the upwelling radiation, T_{up} , from the atmosphere plus the attenuated surface brightness temperature, T_b , and the surface-scattered brightness temperature, T_{sc} . Brightness temperature contributions from the extra-terrestrial sources are grouped in T_{sky} .

and

$$\bar{T}_{ML} = \frac{1}{\bar{G}} \iint_{\text{main lobe}} G(\theta, \phi) T_{AP}(\theta, \phi) d\theta d\phi \quad (6.7)$$

$$\bar{T}_{SL} = \frac{1}{\bar{G}} \iint_{\text{side lobes}} G(\theta, \phi) T_{AP}(\theta, \phi) d\theta d\phi. \quad (6.8)$$

For downward-looking radiometers, the apparent brightness temperature distribution includes contributions from the surface and the intervening atmosphere (Ulaby et al., 1981). For a spaceborne sensor this can be expressed as,

$$T_{AP}(\theta, \phi) = [T_b(\theta, \phi) + T_{sc}(\theta, \phi)]e^{-\tau \sec \theta} + T_{up}(\theta) \quad (6.9)$$

where $T_b(\theta, \phi)$ is the surface brightness temperature, $T_{sc}(\theta, \phi)$ is the surface scattering temperature, τ is the total effective optical depth of the atmosphere and T_{up} is the effective atmospheric upwelling temperature. T_{up} is the effective radiometric temperature of the atmosphere which depends on the temperature and density profile, atmospheric losses, clouds, etc. (Janssen, 1993). The situation is modified somewhat for upward-looking radiometers since there is little surface contribution.

Ignoring incidence and azimuth angle dependence, the surface brightness temperature is given by,

$$T_b = \epsilon T_P \quad (6.10)$$

where ϵ is the emissivity of the surface and T_P is the physical temperature of the surface. The emissivity is a function of the surface roughness and the permittivity of the surface which are related to the geophysical properties of the surface (Ulaby et al., 1981).

The surface brightness temperature, $T_{sc}(\theta, \phi)$, is the result of downwelling atmospheric emissions which are scattered off of the rough surface toward the sensor. This signal depends on the scattering properties of the surface (surface roughness and dielectric constant) as well as the atmospheric emissions directed toward the ground. Note that azimuth variation with brightness temperature has been observed over the ocean (Wentz, 1992), sand dunes (Stephen and Long, 2005), and snow in Antarctica (Long and Drinkwater, 2000).

The total effective optical depth of the atmosphere, τ , corresponds to the signal loss from the surface vertically through the atmosphere. This depends on the frequency, density profile, and other atmospheric factors. Given the atmospheric density, temperature, cloud and liquid water profile, τ , T_{sc} , and T_{up} can be computed using radiative transfer techniques (Ulaby et al., 1981). Note that these are dependent on frequency and polarization. By making multiple channel (i.e. several measurements at different frequencies and electromagnetic polarizations), key parameters of the atmospheric profile can be determined by inverting the radiative transfer equations (Cherny and Raizer, 1998; Janssen, 1993; Ulaby et al., 1981).

Radiometer measurements are “noisy” due to the limited integration time available for each measurement. The uncertainty is expressed as ΔT , which is the standard deviation of the temperature measurement. ΔT is a function of the integration time and bandwidth used to make the radiometric measurement and is typically inversely related to the time-bandwidth product (Ulaby et al., 1981). Increasing the integration time and/or bandwidth reduces ΔT . High stability and precise calibration of the system gain is required to accurately infer the brightness temperature T_b from the sensor power measurement P_{SYS} .

A wide variety of techniques are used to provide the required calibration (Ulaby et al., 1981). A Dicke radiometer periodically switches a known power noise

source into the receiver to measure the gain. Total power radiometers avoid the switching but use antenna rotation to point the antenna at deep space (which is cold) and/or warm calibration targets to provide reference calibration measurements.

6.2.1.2 Polarimetric Radiometry

In polarimetric radiometry multiple polarization emissions are measured and cross-correlated. In polarimetric radiometry the observed brightness temperature $T_{b,p}$ at polarization p is related to the physical temperature (radiance) T_P by the polarization-dependent emissivity ϵ_p according to

$$T_{b,p} = \epsilon_p(\theta, \phi)T_P \quad (6.11)$$

where θ and ϕ are the viewing geometry parameters. The emissivity depends on the physical properties of the medium, including the dielectric constant and surface roughness. In this expression, p can be v , h , 45 , -45 , lc , or rc , corresponding to vertical, horizontal, plus 45° , minus 45° , left-hand circular, and right-hand circular polarizations, respectively. These polarizations are computed by taking the appropriate averages of the observed electric field correlations.

The modified Stokes vector I_s ,

$$I_s = \begin{bmatrix} I \\ Q \\ U \\ V \end{bmatrix} = \begin{bmatrix} T_v \\ T_h \\ T_{45} - T_{-45} \\ T_{lc} - T_{rc} \end{bmatrix} = \begin{bmatrix} \langle E_v E_v^* \rangle \\ \langle E_h E_h^* \rangle \\ 2\text{Re}\langle E_v E_h^* \rangle \\ 2\text{Im}\langle E_v E_y^* \rangle \end{bmatrix} \quad (6.12)$$

where the $\langle \rangle$ denotes averaging of the enclosed emitted electric fields, provides a full characterization of the electromagnetic signature of the surface. The various terms (I , Q , U , V) depend on both the electrical and mechanical properties (roughness) of the scene (Piepmeier et al., 2007).

An important application of polarimetric radiometry is in ocean wind retrieval (Yueh et al., 1994). The microwave emission from the ocean is wind speed dependent due to the roughening of the surface caused by wind-generated waves. The wave structure also leads to (small) sinusoidal dependence of the emission on the wind direction. While the H and V components of the Stokes vector are in phase, the third (U) and (V) components are out-of-phase with the H and V components, making it possible to retrieve the wind direction with a single azimuth look. Because of the small modulation (a few degrees K), however, the U and V components must be very precisely measured (Gaiser et al., 2004; Hudson et al., 2007; Piepmeier et al., 2007).

6.2.1.3 Scanning Methods

The resolution of a radiometer is defined by the antenna gain pattern, specifically the extent of the mainlobe. Motion during the integration period can smear and degrade the resolution. Radiometric interferometers employ multiple antennas and use the interference patterns to improve the resolution (Wohlleben et al., 1991). In either case, to provide greater angular and/or spatial coverage, the antenna is scanned, either mechanically or electrically. A number of scanning schemes are employed on spacecraft for Earth remote sensing. The three most important are multiple fixed beams, cross-track scanning, and helical scanning, illustrated in Fig. 6.4. In a helical scanning sensor, the antenna is pointed off-nadir and rotated about the nadir vector. As the spacecraft moves, the ground trace of the antenna boresight forms a helix. This is the most common scanning geometry for spaceborne radiometers. It has also been used for the SeaWinds scatterometer. Synthetic aperture radiometers are being developed (Ruf et al., 1988).

6.2.2 Airborne Systems

A large number of radiometer systems have been operated from various aircraft, mostly to support various experiments or as demonstration prototypes for spaceborne sensors. Some, however, are in operational use. For example, NOAA operates the AMSU system aboard its hurricane hunter aircraft to sample and observe weather conditions on its flight into hurricanes. While airborne systems are of great interest, due to limitations of space, they are not considered in this chapter.

6.2.3 Spaceborne Systems

Spaceborne radiometers systems have provided global observations of the earth since the late 1970's and continue to be an important tool for the study of the earth. All though the space environment is severe, with proper design practices systems with the high calibration precision and stability required to ensure the utility of the data. Starting with early scanning systems radiometer technology continues to evolve with the recent addition of fully polarimetric systems such as WindSat. A number of important historical and contemporary spaceborne radiometer systems are described in the next section.

6.3 Earth Observing Spaceborne Radiometer Systems

The goal of this subsection is to summarize basic sensor information about a number of important Earth-looking radiometer systems that have operated aboard spacecraft. Only selected sensors are included.

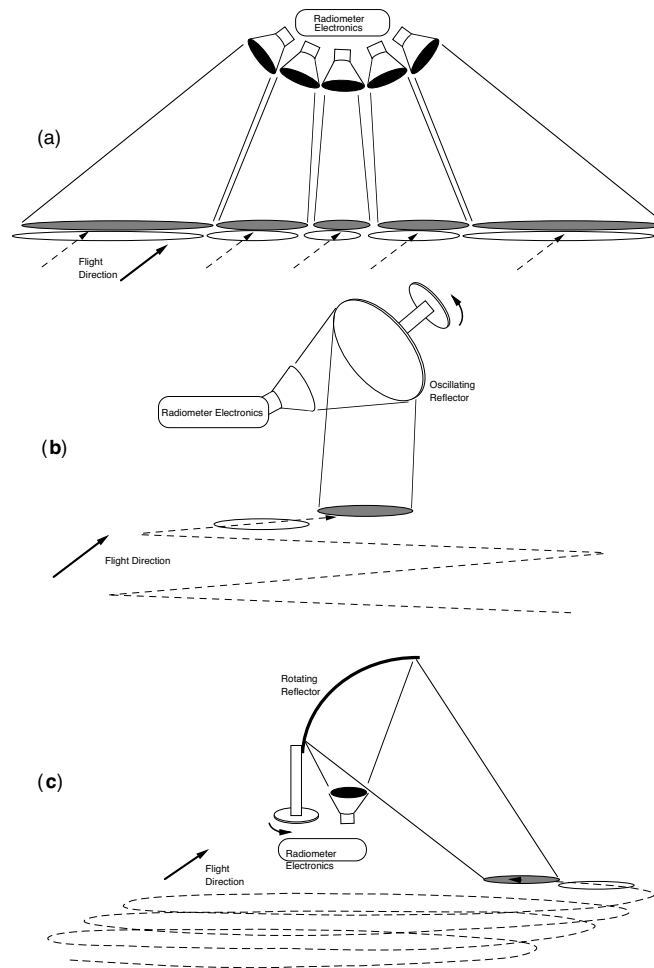


Figure 6.4: Illustration of the main radiometer scanning types: (a) Multiple fixed beams in a "push-broom" configuration; (b) Cross-track scanning with the aid of a scanning reflector; and (c) Helical scanning, which results from spinning the antenna about the nadir axis.

6.3.1 Historical Radiometers

A significant number of short-term experimental radiometer systems have been flown; however, this data is not generally available and so they are not included in this listing. Instead, only the most important of these is listed here.

6.3.1.1 Scanning Multichannel Microwave Radiometer (SMMR)

The SMMR instrument is a five frequency radiometer that first flew on Nimbus-7 and later flew aboard Seasat, both launched in 1978. The inherent resolution of the various SMMR channels varies from a coarse $95 \text{ km} \times 148 \text{ km}$ to as fine as $18 \text{ km} \times 27 \text{ km}$ depending on frequency (Gloersen and Barath, 1977; Njoku et al., 1980). The SMMR was the first successful spaceborne helical scanning radiometer and data from SMMR data has been widely used in a variety of studies, particularly of sea ice properties, including extent and thickness (Gloersen et al., 1987).

Table 6.1: Sensor characteristics of SSMR.

Sensor	SMMR
Sensor Type	Dicke Radiometer
Sensor Scan	helical scan
Polarization	H, V
Center Frequency	6.63, 10.69, 18.0, 21.0, 37.0 GHz
Operating Bandwidth	250 MHz
Radiometric Accuracy (ΔT)	0.4 – 1.1
Coverage	global
Swath Width	780 km
Footprint Shape	elliptical
Footprint Size (Seasat)	$121 \times 79 \text{ km}$, $74 \times 49 \text{ km}$, $44 \times 29 \text{ km}$, $38 \times 24 \text{ km}$, $21 \times 14 \text{ km}$
Incidence Angle	Nimbus-7: 53.3° , Seasat: 49°
Mission Length	Nimbus-7: 1978-1987, Seasat: 1978
Spacecraft	Nimbus-7, Seasat
Orbit	$\sim 800 \text{ km}$ circular sun-synchronous
Fundamental Measurement	Brightness temperature (T_b)
Key Products	Sea ice extent and concentration water vapor atmospheric liquid water
Product Resolution	25 km
Data Availability	podaac.jpl.nasa.gov nsidc.org eosweb.larc.nasa.gov

6.3.2 Contemporary Radiometers

A number of important radiometer sensors or series of sensors are currently operating. Data from these sensors are generally available for scientific research. While it is not possible to list all sensors, a number of significant sensors are described.

6.3.2.1 Special Sensor Microwave/Imager (SSM/I)

The SSM/I is a total-power radiometer with seven channels. These channels cover four different frequencies with horizontal and vertical polarizations channels at 19.35, 37.0, and 85.5 GHz and a vertical polarization channel at 22.235 GHz (Hollinger et al., 1990). An integrate-and-dump filter is used to make radiometric brightness temperature measurements as the antenna scans the ground track via antenna rotation (Holliner, 1989). The 3 dB elliptical antenna footprints range

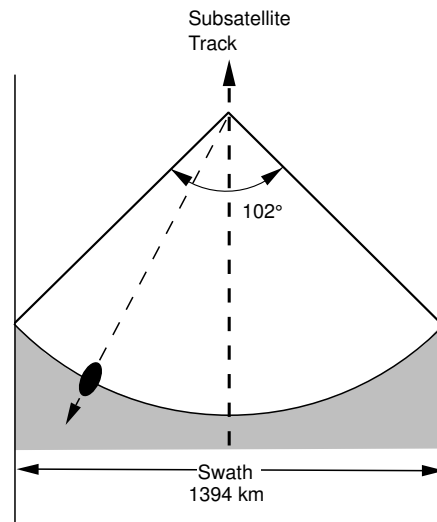


Figure 6.5: An illustration of the SSM/I coverage swath, which consists of a portion of the helical scan of the antenna. The remainder of the scan is used for calibration. The dark ellipse schematically illustrates the antenna mainlobe on the surface for a particular channel which is maintained at a constant incidence angle.

from about 15-70 km in the cross-scan direction and 13-43 km in the along-scan direction depending on frequency (Hollinger et al., 1987). First launched in 1972, SSM/I instruments have flown on multiple spacecraft continuously until the present (2008) on the Defense Meteorological Satellite Program (DMSP) (F) satellite se-

ries. The scanning geometry results in a swath diagram as shown in Fig. 6.5. With its multiple sensors, the extensive SSM/I dataset provides a critical database for studies of long-term climate change, including atmospheric moisture, rainfall, air-sea interaction, and surface wind speed (see, for example, (Berg and Kummerow, 2005; Colton and Poe, 1999; Wentz, 1991)). Though originally designed for atmospheric sensing, SSM/I data has been extensively used for studies of sea ice and other applications (Ferraro et al., 1996).

Table 6.2: Sensor characteristics of SSM/I.

Sensor	SSM/I
Sensor Type	Radiometer
Sensor Scan	helical scan
Polarization	19.35, 37, 85.5 : H, V 22.23 : V
Center Frequency	19.35, 22.23, 37, 85.5 GHz
Operating Bandwidth	125, 300, 750, 500, 2000 MHz
Radiometric Accuracy (ΔT)	1.0 to 0.3
Coverage	global
Swath Width	1400 km
Footprint Shape	elliptical
Footprint Size	43×69 km, 43×69 km, 60×40 km, 37×28 km, 37×20 km, 15×13 km, 15×13 km
Incidence Angle	~ 53°, 49.9° for 10.7 GHz
Mission Length	1972 to present
Spacecraft	DMSP F series
Orbit	805 km circular sun-synchronous
Fundamental Measurement	Brightness temperature (T_b)
Key Products	wind speed atmospheric temperature rain rate water vapor
Product Resolution	25 km, 12.5 km
Data Availability	www.remss.com www.ncdc.noaa.gov rain.atmos.colorstate.edu/CRDC

6.3.2.2 Microwave Sounding Unit (MSU)

A number of MSU radiometer instruments have been operated on NOAA polar-orbiting platforms. Using fixed beam scanning, the MSU is designed for atmospheric temperature profiling at multiple incidence angles. An extensive database starting from 1979 through the present has been collected.

Table 6.3: Sensor characteristics of MSU.

Sensor	MSU
Sensor Type	microwave sounder
Sensor Scan	multiple fixed beams 11 cross-track observation points
Center Frequency	50.3–57.95 GHz
Coverage	global
Incidence Angle	0, 11, 22, 33, 44 and 55 deg
Mission Length	1979 to present
Spacecraft	TIROS-N NOAA Polar platforms
Fundamental Measurement	Brightness temperature (T_b)
Key Products	atmospheric temperature profiles
Data Availability	www.remss.com www.doc.jaxa.jp

6.3.2.3 Advanced Microwave Sounding Unit (AMSU)

AMSU is a multi-channel microwave sounder designed primarily to obtain temperature and humidity profiles in the upper atmosphere (especially the stratosphere) and to provide a cloud-filtering capability for tropospheric temperature observations. The first AMSU was launched in May 1998 on board the DMSP F-15 (now NOAA 15) satellite and has flown on NOAA 16 and 17. AMSU is similar to MSU but includes additional channels. An advanced version known as the Advanced Technology Microwave Sounder (ATMS) is planned for the NPOES mission (Goldberg et al., 2006).

AMSU consists of two instruments: AMSU-A with 15 channels and AMSU-B with 5 channels. AMSU-A is designed primarily for atmospheric temperature profiling and thus has many narrow channels. AMSU-B is designed for moisture profiling, but has other applications. For example, the observations can also be for land surface cover studies (Karbou, 2005; Karbou et al., 2005) and snow cover (Kongoli et al., 2003).

Table 6.4: AMSU-A & AMSU-B Frequencies (GHz) and Channels

Channel	AMSU-A	AMSU-B
1	23.8	89.0
2	31.4	150.0
3	50.3	183.3±1
4	52.8	183.3±3
5	53.6	183.3±7
6	54.4	
7	54.9	
8	55.5	
9	57.2	
10-14	57.29 ±.217 & ±.322	
15	89.0	

Notation: $x \pm y$ where x is the center frequency. If y appears, the measurements are made in two bands on either side of the center frequency and y is the distance of the passbands to the center frequency

[<http://amsu.cira.colostate.edu>].

Table 6.5: Sensor characteristics for AMSU.

Sensor	AMSU
Sensor Type	microwave sounder
Sensor Scan	cross-track scan
Center Frequency	AMSU-A: 15 channels 15-90 GHz
Coverage	global
Swath Width	1650 km
Footprint Shape	variable, elliptical
Mission Length	1998 to present
Spacecraft	NOAA platforms NASA Aqua platform
Orbit	833 km circular sun-synchronous 101 min period 98.7° inclination angle
Fundamental Measurement	Brightness temperature (T_b)
Key Products	atmospheric temperature profiles
Product Range	5 levels to 40 km
Data Availability	www.remss.com www.orbit.nesdis.noaa.gov amsu.cira.colostate.edu ghrc.msfc.nasa.gov

6.3.2.4 Tropical Rain Measuring Mission (TRMM) Microwave Imager (TMI)

TMI was launched in 1995 as part of the TRMM mission (Awaka et al., 1997; Meneghini et al., 2000). The conically scanning TMI measured radiometric emissions in several microwave channels and polarizations designed for measuring atmospheric moisture and rain over a wide swath. TRMM has far exceeded its design life and has provided an extensive data set over the tropics (latitude less than $\pm 30^\circ$). Designed for a 350 km altitude, the TRMM orbit altitude was raised in 2001 to extend the mission life. TMI data is augmented by TRMM PR data. The TMI 3 dB elliptical antenna footprints range from about 5-8 km in the cross-scan direction and 7-63 km in the along-scan direction depending on frequency. The scanning geometry results in the swath diagram as shown in Fig. 6.6 at the 350 km orbit height.

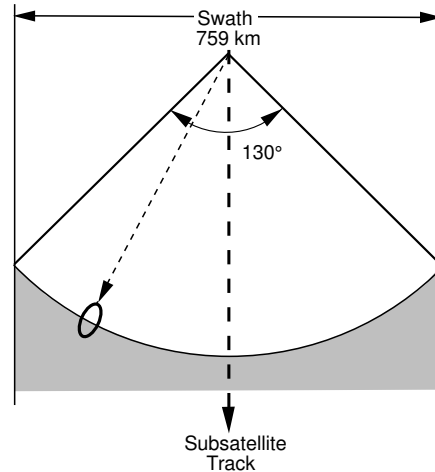


Figure 6.6: An illustration of the TMI coverage swath, which consists of a portion of the helical scan of the antenna. The remainder of the scan is used for calibration. The observation incidence angle is essentially constant.

Table 6.6: Sensor characteristics for TMI.

Sensor	TMI
Sensor Type	Radiometer
Sensor Scan	helical scan
Polarization	V & H (except 21.3 GHz which V only)
Center Frequency	10.7, 19.4, 21.3, 37, 85.5 GHz
Coverage	40S to 40N
Swath Width	780 km
Footprint Shape	elliptical
Footprint Size	45 km to 5 km
Incidence Angle	52.8°
Mission Length	Dec. 1995 to present
Spacecraft	TRMM
Orbit	350 & 400 km circular, semi-equatorial 35° inclination angle non-sun synchronous
Fundamental Measurement	Brightness temperature (T_b)
Key Products	sea surface temperature ocean wind speed water vapor cloud water rain rate water vapor
Product Resolution	25 km
Data Availability	gsfc.nasa.com www.remss.com

6.3.2.5 Microwave Scanning Radiometer (MSR)

The MSR flew aboard the Japanese Marine Observation Satellite-1 (MOS-1) launched in 1987 and aboard the follow-on MOS-1b in 1990 (Maeda et al., 1989). MSR data can be used infer to sea surface temperature (SST) (Takeuchi et al., 1993).

Table 6.7: Sensor characteristics for MST.

Sensor	MSR
Sensor Type	Radiometer
Sensor Scan	helical scan
Polarization	H, V
Center Frequency	12, 31 GHz
Coverage	global
Swath Width	320 km
Footprint Shape	elliptical
Mission Length	MOS-1: Feb. 1987 – Nov. 1995 MOS-1: Feb. 1990 – Apr. 1996
Spacecraft	MOS-1, MOS-1b
Orbit	909 km circular sun-synchronous 103 min period 99° inclination angle
Fundamental Measurement	Brightness temperature (T_b)
Key Products	sea surface wind speed sea surface temperature integrated water vapor snow fall
Product Resolution	32 km, 23 km
Data Availability	www.eorc.jaxa.jp www.doc.jaxa.jp

6.3.2.6 Advanced Microwave Scanning Radiometer (AMSR and AMSR-E)

The Japanese Aerospace Exploration Agency (JAXA) developed the design for AMSR for the ADEOS-II mission. AMSR first flew on ADEOS-II which operated from Jan. 2003 through Oct. 2003 before the mission prematurely terminated due to loss of spacecraft power. A second instrument, denoted AMSR-E, was launched aboard the U.S. Aqua mission. AMSR-E is similar to AMSR but does not include 50 MHz channels (Kwanishi et al., 2003). AMSR-E employs a 1.6 m offset parabolic dish antenna which is conically scanned. Some radio frequency interference has been observed in the 6.9 GHz and 10.65 GHz channels (Li et al., 2004; Njoku et al., 2005). The data is widely used for a variety of oceanographic, atmospheric, cryosphere, and land studies. The AMSR scanning geometry results fixed incidence angle observations over the swath as diagramed in Fig. 6.7

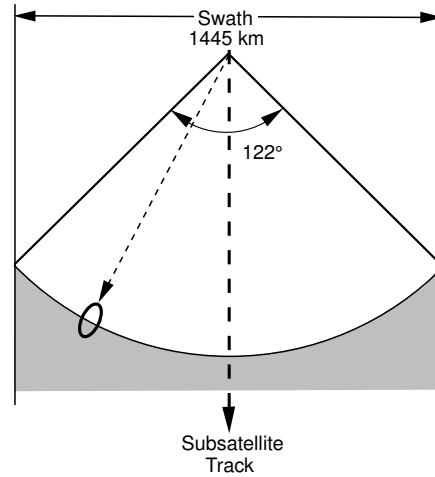


Figure 6.7: An illustration of the AMSR coverage swath, which consists of a portion of the helical scan of the antenna. The remainder of the scan is used for calibration. The observation incidence angle is essentially constant.

Table 6.8: Sensor characteristics for AMSR and AMSR-E.

Sensor	AMSR & AMSR-E
Sensor Type	Radiometer
Sensor Scan	helical scan
Polarization	H, V
Center Frequency	AMSR: 50.3 and 52.8 are V-only 6.925, 10.65, 18.7, 23.8, 36.5, 89.0 GHz
Operating Bandwidth	AMSR: 50.3 and 52.8 GHz 360,100,200,400, 1000, 3000 MHz
Radiometric Accuracy (ΔT)	0.3 K, 0.6 K, 0.6 K, 0.6 K, 0.6 K, 1.1K AMSR: 2K for 50.3 and 52.8 GHz
Coverage	global
Swath Width	AMSR 1600 km AMSR-E 1450 km
Footprint Shape	elliptical
Footprint Size	75×43 km, 51×29 km, 27×16 km, 32×18 km, 14×8 km, 6×4 km
Incidence Angle	~ 55°
Mission Length	AMSR: Jan-Oct 2003 AMSR-E: May 2002 to present
Spacecraft	AMSR: ADEOS-II (Midori-2) AMSR-E: Aqua
Orbit	AMSR: 805 km circular sun-synchronous AMSR-E: 705 km circular sun-synchronous
Fundamental Measurement	Brightness temperature (T_b)
Key Products	sea surface wind speed sea surface temperature integrated cloud liquid water precipitation sea ice concentration integrated water vapor snow depth soil moisture
Data Availability	www.eorc.jaxa.jp www.remss.com

6.3.2.7 WindSat

The WindSat/Coriolis mission carries the first orbital polarimetric radiometer. The WindSat radiometer is the testbed for a new series of radiometers to be flown aboard the National Polar-orbiting Operational Environmental Satellite System (NPOESS) (Gaiser et al., 2004). WindSat is designed to evaluate the viability of polarimetric radiometry for measuring the speed and direction of ocean winds from space. WindSat includes multiple polarimetric and dual-polarized channels sharing a 1.8 m offset reflector antenna. The scanning geometry was selected to evaluate both single look and dual azimuth retrieval of wind speed and direction (Gaiser et al., 2004). The data can also be used to observe sea surface temperature, rain, cloud liquid water, soil moisture, and other variables (Lee et al., 2005; Windsat, 2007).

The scanning geometry of WindSat is designed to make both forward and aft-facing T_b measurements over part of its observation swath (see Fig. 6.8) in order to evaluate the potential of using the azimuth dependence of T_b to retrieve near-surface ocean winds from the measurements.

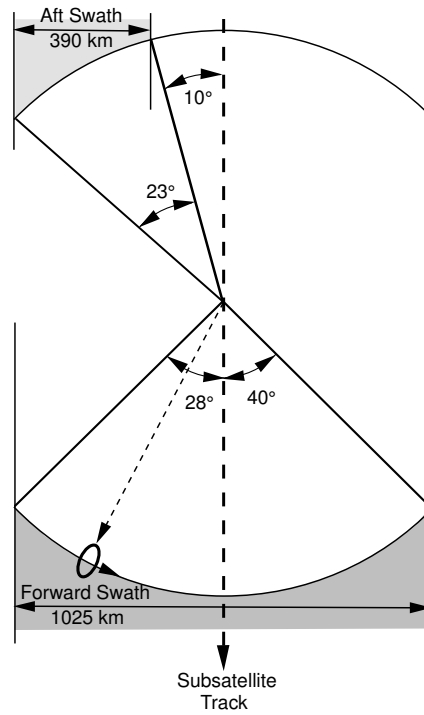


Figure 6.8: An illustration of the WindSat overviation geometry and coverage as seen from above. The antenna helically scans the surface at a constant incidence angle. The remainder of the azimuth angles are used for calibration.

Table 6.9: Sensor characteristics for WindSat.

Sensor	WindSat
Sensor Type	Polarimetric radiometer
Sensor Scan	helical scan
Polarization	10.7, 18.7, 37 : H, V, ± 14 , L, R 6.8, 23.8 : H, V
Center Frequency	6.8, 10.7, 18.7, 23.8 37.0 GHz
Operating Bandwidth	125, 300, 750, 500, 2000 MHz
Radiometric Accuracy (ΔT)	0.05 K (12 sec integration)
Radiometric Stability ($\pm T$)	0.12 K (8 days)
Coverage	global
Swath Width	1025 km
Footprint Shape	elliptical
Footprint Size	40 \times 60 km, 25 \times 38 km, 16 \times 27 km, 12 \times 20 km, 8 \times 13 km
Incidence Angle	$\sim 53^\circ$, 49.9° for 10.7 GHz
Mission Length	Jan. 2003 to present
Spacecraft	Coriolis
Orbit	830 km circular sun-synchronous
Fundamental Measurement	Brightness temperature (T_b)
Key Products	ocean wind vectors (primary) sea surface temperature soil moisture rain rate water vapor
Product Resolution	25 km
Data Availability	podaac.jpl.nasa.gov manati.orbit.nesdis.noaa.gov www.nrl.navy.mil/WindSat

6.3.2.8 Multi-frequency Scanning Microwave Radiometer (MSMR)

The MSMSR a four frequency dual-polarization radiometer that is broadly similar to SMMR. Developed by India, it was first launched on the India Research Satellite (IRS) P-4 in May 1999. Another MSMR flies onboard the Indian OCEANSAT-1 (Bhandari et al., 2002; Misra et al., 2002). MSMR has been used extensively for the study of sea ice (Vyas and Dash, 2000; Vyas et al., 2004).

Table 6.10: Sensor characteristics of MSMR.

Sensor	MSMR
Sensor Type	Radiometer
Sensor Scan	helical scan, 11.173 RPM
Polarization	H, V
Center Frequency	6.6, 10.65, 18, 21 GHz
Coverage	global
Swath Width	1350 km
Footprint Shape	elliptical
Incidence Angle	49.7°
Mission Length	1999 to present
Spacecraft	IRS P-4, OCEANSAT-1
Orbit	720 km circular sun-synchronous 98.28° inclination angle 12:00 ascending node
Fundamental Measurement	Brightness temperature (T_b)
Key Products	wind speed atmospheric temperature rain rate water vapor
Product Resolution	150, 75, 50, 60 km
Data Availability	www.remss.com

6.3.3 Planned Radiometer Systems

Many new spaceborne passive microwave sensors are in various planning stages in the U.S., Japan, Europe, China, and India. Some of these are extensions of existing missions, but many new missions are also planned. While it is not possible to include all of these, several important planned systems are described.

6.3.3.1 Aquarius

The Aquarius mission is a joint mission between NASA, which is supplying the sensors, and Argentina, which is supplying the spacecraft. The Aquarius mission includes both an L-band polarimetric radiometer operating at 1.4 GHz and a dual-frequency L-band scatterometer operating at 1.2 GHz to make precise global observations of sea surface salinity from space (Aquarius, 2007). Both sensors share a 2.5 m reflector that employs a helical scanning pattern. Aquarius is scheduled for launch in Sept. 2008. Key instrument parameters are given in the following tables.

Table 6.11: Sensor characteristics for the Aquarius Radiometer.

Sensor	Aquarius Radiometer
Sensor Type	Polarimetric radiometer
Sensor Scan	3 beam helical scan
Polarization	H, V, U
Center Frequency	1.413 GHz
Operating Bandwidth	4 MHz
Net integration time	20 ms and 10 s
Radiometric Accuracy (ΔT)	0.05 K (12 sec integration)
Radiometric Stability ($\pm T$)	0.12 K (8 days)
Coverage	global, every 8 days
Swath Width	340 km
Footprint Shape	elliptical
Footprint Size	62×68 km, 68×82 km, 75×100 km
Incidence Angle	23.3°, 33.7°, 41.7°
Mission Length	Sept. 2008 to Sept. 2011
Orbit	600 km circular sun-synchronous 98° inclination angle 6 pm descending node
Fundamental Measurement	Brightness temperature (T_b)
Key Products*	Monthly ocean salinity map
Product Accuracy	0.2 psu
Product Range	32-37 ppt
Data Availability	(future)

* Aquarius mission product (combined radiometer/scatterometer)

Table 6.12: Sensor characteristics for the Aquarius Scatterometer.

Sensor	Aquarius Scatterometer
Sensor Type	Polarimetric scatterometer
Sensor Scan	single beam helical scan
Polarization	H, V
Center Frequency	1.413 GHz
Pulse Length	1 ms
PRF	100 Hz
Operating Bandwidth	4 MHz
Radiometric Accuracy (K_p)	0.1 dB
Radiometric Stability ($\pm\sigma^o$)	0.13 dB (8 days)
Coverage	global, every 8 days
Swath Width	340 km
Footprint Shape	elliptical
Mission Length	Sept. 2008 to Sept. 2011
Orbit	600 km circular sun-synchronous 98° inclination angle 6 pm descending node
Fundamental Measurement	radar backscatter (σ^o)
Key Products*	Monthly salinity map
Product Accuracy	0.2 psu
Data Availability	(future)

* Aquarius mission product (combined radiometer/scatterometer)

6.3.3.2 Soil Moisture and Ocean Salinity (SMOS)

The SMOS mission will use an L-band 2-d interferometric radiometer to make high resolution measurements of soil moisture and ocean salinity (Font et al., 2000; Kerr et al., 2001). This innovative sensor is scheduled for launch in 2008.

Table 6.13: Sensor characteristics for SMOS.

Sensor	SMOS
Sensor Type	Interferometric radiometer
Polarization	H, V, U
Center Frequency	1.41 GHz
Fundamental Measurement	Brightness temperature (T_b)
Radiometric Accuracy (ΔT)	0.64 K
Coverage	global
Swath Width	1500 km
Footprint Shape	elliptical
Footprint Size	nominally 40 km
Mission Length	2008-2011
Spacecraft	Proteus
Orbit	763 km circular
Key Products	soil moisture ocean salinity
Product Resolution	30-50 km
Product Accuracy	0.1 psu (salinity)
Data Availability	(future)

6.3.3.3 Hydros

The NASA Hydrosphere State (Hydros) mission was to include both an innovative scanning synthetic aperture radar/scatterometer and a radiometer in order to measure soil moisture from orbit (Njoku et al., 2003). Hydros was scheduled for launch in 2010, but has been canceled. It is likely to be rescheduled under a different name.

The mission was to include both an L-band radiometer operating at 1.4 GHz and an L-band SAR/scatterometer operating at 1.2 GHz to make precise global observations of sea surface salinity from space (Aquarius, 2007). Both sensors share a horn feed and 6 m reflector that is helically scanned. Key instrument parameters are given in the following tables.

Soil moisture is retrieved from the radiometer measurements with corrections for soil roughness obtained from the scatterometer (Njoku and Entekhabi, 1996; Njoku et al., 2000). The scatterometer design is based on SAR-type processing of scanning scatterometer data, though low-resolution processing is also planned (Spencer et al., 2003).

Table 6.14: Sensor characteristics for the proposed Hydros Radiometer.

Sensor	Hydros Radiometer
Sensor Type	Polarimetric radiometer
Sensor Scan	single beam helical scan
Polarization	H, V, U
Center Frequency	1.41 GHz
Fundamental Measurement	Brightness temperature (T_b)
Radiometric Accuracy (ΔT)	0.64 K
Coverage	global
Swath Width	1000 km
Footprint Shape	elliptical
Footprint Size	nominally 40 km
Mission Length	Sept. 2011 to 2013
Orbit	670 km circular sun-synchronous 6 am
Key Products*	Monthly soil moisture map Freeze/Thaw state
Product Resolution	3×3 km and 10×10 km
Product Accuracy	±4%
Data Availability	(future)

* mission product (combined radiometer/scatterometer)

Table 6.15: Sensor characteristics for the proposed Hydros Scatterometer.

Sensor	Hydros Scattterometer
Sensor Type	Polarimetric scatterometer
Sensor Scan	single beam helical scan
Polarization	HH, VV, HV
Center Frequency	1.26 GHz
Fundamental Measurement	radar backscatter (σ^0)
Fundamental Resolution	3 km, 10 km, 30 km
Radiometric Stability ($\pm\sigma^0$)	1.0 dB (3 km), 0.45 dB (10 km)
Coverage	global
Swath Width	two 350 km wide swaths separated by 300 km wide gap
Footprint Shape	elliptical
Footprint Size	30 km
Incidence Angle	39.3°
Mission Length	2011 to 2013
Orbit	670 km circular sun-synchronous 6 am
Key Products*	Monthly soil moisture map Freeze/Thaw state
Product Resolution	3×3 km and 10×10 km
Product Accuracy	±4%
Data Availability	(future)

* mission product (combined radiometer/scatterometer)

6.3.3.4 Conical Microwave Imager Sounder (CMIS)

CMIS is a multichannel helically scanning radiometer originally planned for deployment as part of the National Polar-orbiting Operational Environmental Satellite System (NPOESS). Due to program cost overruns, CMIS has been descoped. While it is very likely that NPOESS will include a radiometer, it is not clear precisely what features it will have.

6.3.3.5 Advanced Technology Microwave Sounder (ATMS)

ATMS is the next generation of AMSU instruments and includes some additional channels for a total of 22. A flat, rotating reflector is planned (Goldberg et al., 2006).

6.3.3.6 Global Precipitation Measurement Program (GPM)

The Japanese GPM mission will include a Dual-Frequency Precipitation Radar (DPR) and a Microwave Radiometer Imager (GMI). The DPR consists of a TRMM/PR weather radar operating at 13.6 GHz with an added 34.5 GHz precipitation radar.

The 13.6 GHz channel will have a swath width of 245 km while the 34.5 GHz channel will have a narrower swath of about 100 km.

GMI will be a nine channel radiometer similar to the TRMM Microwave Imager (TMI), but with fewer channels and a smaller (1.2 m) antenna. It will have a 800 km wide swath. GMI is designed to support rain observation and will be deployed on the GPM satellite operating at 400 km altitude.

6.3.4 Extra-Terrestrial Radiometer Sensors

While most radio astronomy has been done from ground-based radio telescopes, several spaceborne radiometers systems have flown to observe extra-terrestrial phenomena. Of particular note are missions to map the cosmic background radiation at microwave frequencies. The cosmic background radiation is a low level (about 2.7 K) brightness temperature that permeates deep space. It is believed to originate from the big bang (Bennett et al., 1996). Originally thought to be isotropic, very precise radiometers have found very small anisotropies in the cosmic background radiation which are thought to be the result of turbulence in the early universe (Levi, 1992). Several microwave sensors designed to map these anisotropies in the cosmic background radiation are described below.

6.3.4.1 COBE DMR

The Cosmic Background Explorer (COBE) mission carried a number of sensors to study the cosmic background radiation (CBR). One of its key sensors was the Differential Microwave Radiometers (DMR), which consists of six differential radiometers that operate in pairs (Smoot et al., 1990). Pointing in different directions, the difference between the signals in each antenna is recorded to map anisotropy in the CBR. To achieve the extreme precision, a careful differential radiometric measurement scheme is used for the receivers.

Table 6.16: Sensor characteristics for COBE.

Sensor	COBE DMR
Sensor Type	paired differential radiometer
Sensor Scan	precessing helical scan
Polarization	circular
Center Frequency	31.5, 53, & 90 GHz
Fundamental Measurement	Differential brightness temperature (dT_b)
Coverage	full-sky
Mission Length	1989 to 1993
Spacecraft	COBE
Orbit	900 km circular polar
Key Products*	Differential T_b map
Product Accuracy	3.3 mK%
Data Availability	lambda.gsfc.nasa.gov/product/cobe

* one of several mission products

6.3.4.2 Relikt

The Soviet Prognoz 9 mission included the Relikt-1 radiometer to measure the CMB using a single channel radiometer (Strukov et al., 1992).

Table 6.17: Sensor characteristics for Relikt.

Sensor	Relikt
Sensor Type	radiometer
Center Frequency	37 GHz
Fundamental Measurement	brightness temperature (T_b)
Coverage	full-sky
Mission Length	1983-1984
Spacecraft	Prognoz 9
Orbit	high apogee, 700,000 km
Product Resolution	5.5°
Product Accuracy	0.6 mK%
Data Availability	lambda.gsfc.nasa.gov/product

6.3.4.3 Wilkinson Microwave Anisotropy Probe (WMAP)

WMAP is a follow-on mission to the COBE mission to COBE [map.gsfc.nasa.gov]. It uses additional microwave channels and provides finer angular resolution of the CBR anisotropy, to 13 arcminutes (Spergel et al., 2003).

Table 6.18: Sensor characteristics for WMAP.

Sensor	WMAP
Sensor Type	differential radiometer
Sensor Scan	precessing helical scan
Polarization	multi
Center Frequency	22,30, 40, 60, & 90 GHz
Fundamental Measurement	Differential brightness temperature (dT_b)
Coverage	full-sky
Mission Length	Oct. 2001 to present
Spacecraft	WMAP
Orbit	Earth-Lunar L2
Key Products*	Differential T_b map
Product Resolution	$0.3^\circ \times 0.3^\circ$
Product Accuracy	$35 \mu\text{K}\%$
Data Availability	lambda.gsfc.nasa.gov/product/map

* one of several mission products

6.4 Active Systems (Radars)

Unlike radiometers which are receive-only devices, radar systems include a transmitter. Scene properties are inferred from the echo of the transmitted signal rather than the radiometric emissions of the surface. Indeed, the radiometric scene emission is “noise” to the radar which is interested in the echo of the transmitted signal.

6.4.1 Introduction

Radar systems can be divided into two types: real-aperture and synthetic aperture radar (SAR) systems. In the latter, resolution is improved by using coherent time/Doppler processing, multiple transmit pulses, and a moving platform to, in effect, synthesize a larger antenna than the physical antenna. This requires significant computation, high bandwidth, and high transmit power, resulting in greater expense. Typically, synthetic aperture radars are more difficult to calibrate (Freeman, 1992) than real aperture radars. SAR systems can provide the highest resolution microwave measurements.

6.4.2 Radar Fundamentals

Radar is an acronym for radio detection and ranging that was coined during its early development. Early radars were used for detection of ships and aircraft. Soon it was noticed that radar signals provide information about the environment and radar-based environmental remote sensing was born.

Radars operate by transmitting a radio signal toward the target or scene of interest and measuring the properties of the returned echo. Unlike radiometers or optical sensors, radar signals are coherent, that is, frequency and phase of the signal are preserved. This property can be exploited to yield more information about the target than is possible with incoherent sensors.

Most radars are pulsed, that is, short pulses of radio signal are individually transmitted and received. The transmitted pulse can be an unmodulated signal known as continuous wave (CW) [sometimes, as interrupted continuous wave (ICW)] or modulated to permit improved range resolution. A common modulation scheme is linear frequency modulation (LFM), sometimes referred to as “chirping”. Figure 6.9 illustrates a system block diagram of a typical radar.

The return echo from the scene consists of attenuated, time-delayed, frequency-shifted copies of the transmitted signal. The time delay arises due to finite speed of light and the range (sometimes referred to as the slant range) between the radar and the scene. Relative motion between the radar and scene give rise to a frequency shift due to the Doppler effect. Attenuation results from the distance and the radar

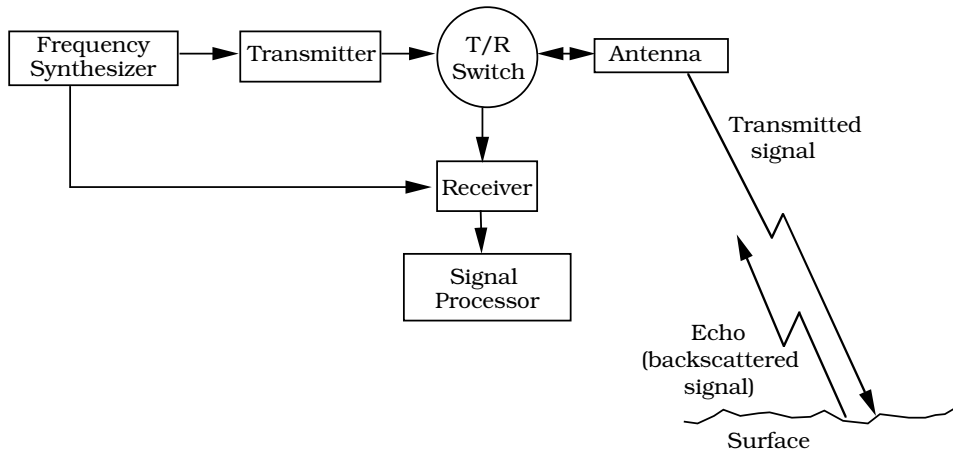


Figure 6.9: General block diagram of a typical spaceborne radar system.

scattering properties of the scene. The radar can thus observe and measure (1) distance via signal time-of-flight, (2) speed via the Doppler effect, and (3) surface scattering. The coherent nature of the signal can lead to self interference from different parts of the illuminated scene.

Some remote sensing radars use all three of these fundamental observations while others use only one. For example, altimeters primarily observe time-of-flight while scatterometers focus on scattering. Altimeters and scatterometers are typically real-aperture systems, meaning that their spatial resolution is determined primarily by the antenna illumination footprint whereas SARs exploit time-of-flight and Doppler to provide higher resolution measurements of the radar scattering.

6.4.3 Real-aperture Radars

Real-aperture remote sensing radars include altimeters, scatterometers, and weather radars. A brief introduction to the operation and theory of these sensors is provided in the following. Side-looking airborne radars (SLARs) are considered later along with SARs.

6.4.3.1 Radar Altimetry

Altimeters are standard equipment on aircraft and are used for measuring the height of the aircraft over the ground. In this application, they are primarily used for navigation. Altimeters used for remote sensing have been primarily used over the ocean and the polar regions of the earth. Here we focus on these applications.

Altimeters are nadir looking instruments. An altimeter transmits a short, generally modulated, pulse toward the surface (see Fig. 6.10). By measuring the time of flight of the return echo, and by knowing the speed of light in the transmission medium, the distance can be determined. The most sophisticated altimeters observe the power versus time profile and use the general measurement geometry to make more precise distance measurements (see Fig. 6.11). With precise knowledge of the orbit, the height of the altimeter over the surface can be determined, enabling mapping of the surface topography. Over the ocean the surface topography can be related to subsurface topography and ocean currents. Variations in sea surface topography provide information on large-scale weather and climate such as El Nino (Fu et al., 1994).

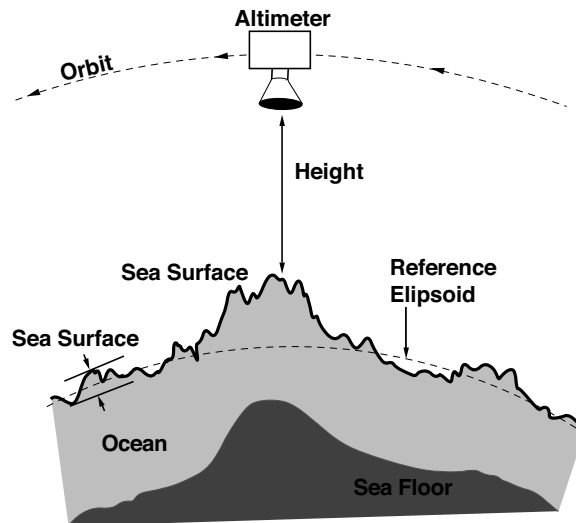


Figure 6.10: Spaceborne altimeter measurement diagram. Precise measurements of the height coupled with precise orbit prediction enable very precise estimation of the surface height relative to the reference ellipsoid.

The shape of the altimeter return pulse is related to the significant wave height, which can thus be inferred from the power versus time measurements. Significant wave height is a measure of large waves on the surface. The received echo power

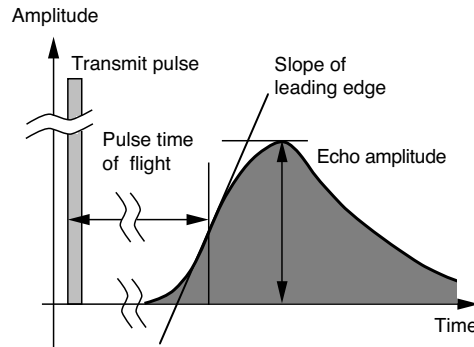


Figure 6.11: Pulse shape information for a spaceborne altimeter measurement over the ocean. From the time of flight measurement, the altimeter height is computed. The peak amplitude of the echo is related to the near-surface wind speed. The slope of the leading edge is related to the significant wave height.

can be converted to scattering measurements for use in inferring the near-surface wind speed over the ocean (Fu et al., 1994, 2001). The altimeter height measurements can also be used to measure glacial ice topography (Martin et al., 1983).

6.4.3.2 Radar Scatterometry

A radar scatterometer is designed to determine the normalized radar cross section (σ^o) of the surface. In primary application these σ^o measurements over the ocean are used to estimate the near-surface vector wind.

The scatterometer does not directly measure σ^o , but instead, measures the backscattered power of a transmitted pulse. Due to thermal noise in the receiver, radiometric noise and speckle, the power measurements are corrupted by noise. A separate measurement of the noise-only power is made and subtracted from the signal+noise measurement to yield a backscatter power “signal” measurement P_S . σ^o is computed from the signal power measurement using the radar equation (Ulaby et al., 1981),

$$\sigma_o = \frac{(4\pi)^3 R^4 L}{P_t G^2 \lambda^2 A} P_S = X P_S \quad (6.13)$$

where R is the slant range to the surface, P_t is the transmitted power, P_S is the received backscattered power, L represents known system losses, G is antenna gain, A is the resolution element area, and λ is the wavelength of the transmitted radiation. R , G , and A depend on the measurement geometry of each resolution

element (see Fig. 6.9). The measurement signal to noise ratio (SNR) depends on the surface σ^o but may vary from -20 to 50 dB.

The scatterometer measurement includes errors due to the uncertainty in the geometric parameters (i.e., in X) as well as noise due to the finite times used to estimate P_S (Fischer, 1972). A common model for the actual value of σ^o , $\sigma^o(k)$, observed by the scatterometer is

$$\sigma^o(k) = \sigma_m^o(k)[1 + K_p(k)\nu(k)] \quad (6.14)$$

where $\sigma_m^o(k)$ is the actual σ^o of the surface for the k^{th} measurement, $K_p(k)$ is the normalized standard deviation of the measurement errors, and $\nu(k)$ is a normally-distributed Gaussian random variable. K_p is sometimes known as the scatterometer “radiometric accuracy”. The multiplication in Eq. (6.14) arises, in part, as a result of speckle noise, an inherent limitation in coherent radars. The K_p in Eq. 6.14 does not include the effects of “model” errors, i.e., variations in the observed σ^o due to very small-scale spatial variations in σ^o related to inhomogeneities in the observed surface. This effectively increases the measurement K_p (uncertainty).

The primary application of spaceborne scatterometry has been measuring near-surface winds over the ocean. By combining σ^o measurements from different azimuth angles, the near-surface wind vector over the ocean’s surface can be determined using a geophysical model function (GMF) which relates wind and σ^o (Naderi et al., 1991). An illustration of the GMF at Ku-band is shown in Fig. 6.12.

More recently, scatterometer data has been used for studies of land, vegetation and polar ice (Long et al., 2001). Because of the sensitivity of the radar backscatter to liquid water, scatterometer data has been particularly useful in polar climate studies, see for example, (Figa-Saldaña et al., 2002; Long and Drinkwater, 1999).

SASS, NSCAT and ESCAT were fan-beam scatterometers while SeaWinds employs a dual rotating pencil-beam antenna (see Fig. 6.14). In a fan-beam scatterometer, along-track resolution results from a combination of a narrow antenna pattern and the timing of transmit pulses integrated into a single measurement cell. Cross-track resolution is obtained either by range gate filtering (ESCAT) or by Doppler filtering (SASS and NSCAT), and the narrow beam pattern.

Range gating is used to achieve along-beam resolution for ESCAT while Doppler filtering is used for SASS and NSCAT. For ESCAT, short, high-power transmit pulses are issued. By selectively integrating the return signal over a narrow time window, only the return echo from a small along-beam resolution element will be included in the integrated power measurement (see Fig. 6.15). For SASS and NSCAT, Doppler filters define along-beam resolution. SASS used fixed filters while NSCAT used variable center frequency filters to maintain measurements at a fixed cross-track position (Naderi et al., 1991). The SASS and NSCAT Doppler fil-

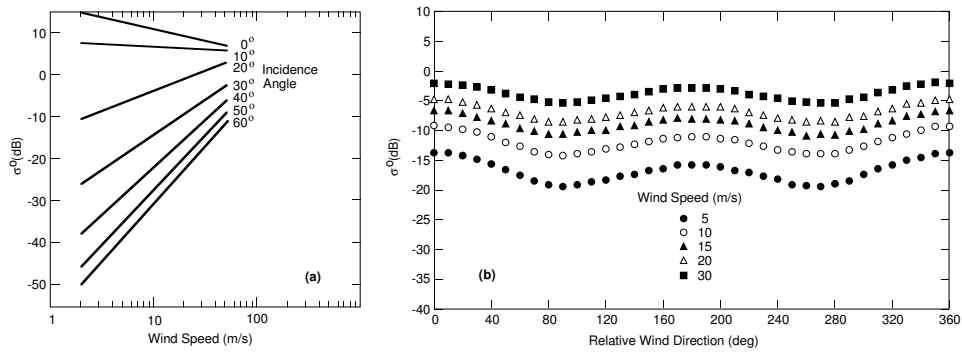


Figure 6.12: The geophysical model function relating near-surface winds and radar backscatter at Ku-band. (a) Radar backscatter versus wind speed at different incidence angles and a fixed wind direction. (b) Radar backscatter versus relative wind direction (the direction difference between the wind and the azimuthal radar look direction) for several wind speeds at a fixed incidence angle. By measuring the backscatter at a point from several different azimuth angles, the vector wind (speed and direction) can be estimated.

tering approaches preclude the use of an antenna at precisely 90° to the along-track velocity vector as used for ESCAT.

Measurement timing is used to achieve along-track resolution. Ideally the centers of resolution cells are spaced approximately 25 km for NSCAT and 50 km for SASS apart in the along-track direction choosing the pulse repetition frequency and number of pulses integrated so that the spacecraft moves 25 km [50 km for SASS] between measurements. A series of pulses are integrated into one σ^0 measurement.

To contrast and compare the Doppler and ranging approaches used by the ERS scatterometer and SASS/NSCAT, consider Fig. 6.16 which compares the SASS/NSCAT antenna illumination pattern of a forward looking fan-beam antenna super-imposed on isoDoppler lines on the Earth's surface and range-compression resolution based on iso-range lines. In Doppler filtering-based resolution a long (1.5 ms) CW pulse is transmitted, resulting in a Doppler/time history plot as is illustrated in Fig. 6.17. The return echo has a Doppler shift related to the along-beam distance. A band-pass filter corresponds to a resolution element defined by the Doppler frequencies and the narrow beamwidth. We note that this approach cannot be used when the antenna is aligned perpendicular to the flight track where the Doppler shift is minimized.

The alternate approach to achieving along-beam resolution, is to use range-

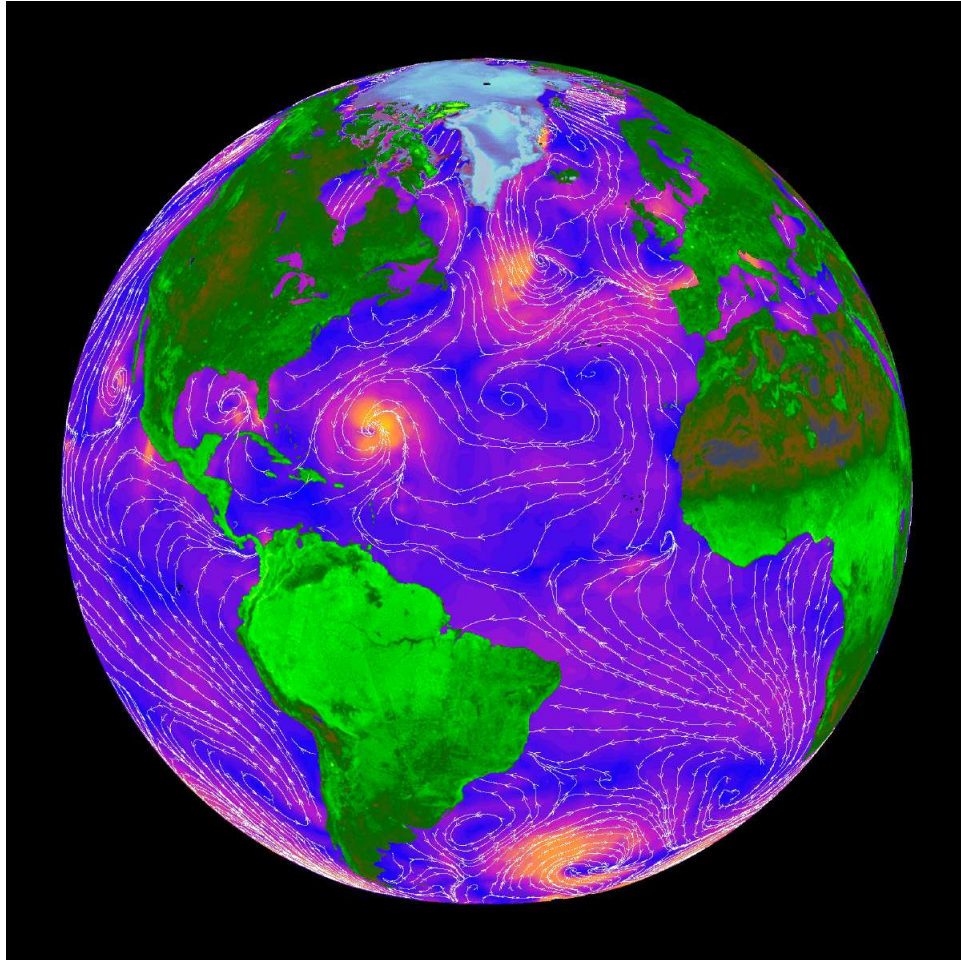


Figure 6.13: False-color image of the Earth generated from Ku-band scatterometer data. Colors over land and ice covered regions correspond to the intensity of the radar backscatter. Over the ocean, colors correspond to the wind speed estimated from the scatterometer measurements with yellow being high speeds and blue low speeds. The white streamlines show the wind direction.

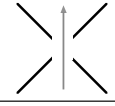
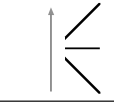
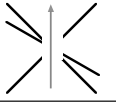
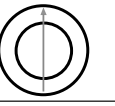
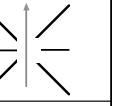
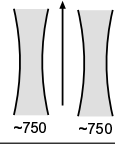
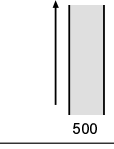
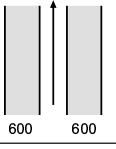
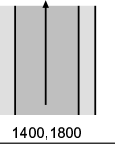
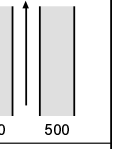
	SASS	ESCAT	NSCAT	SeaWinds	ASCAT
FREQUENCY	14.6 GHz	5.3 GHz	13.995 GHz	13.6 GHz	5.3 GHz
ANTENNA AZIMUTHS					
POLARIZATIONS	V-H, V-H	V ONLY	V, V-H, V	V-OUTER/H-INNER	V ONLY
BEAM RESOLUTION	FIXED DOPPLER	RANGE GATE	VARIABLE DOPPLER	PENCIL-BEAM	RANGE GATE
SCIENCE MODES	MANY	SAR, WIND	WIND ONLY	WIND/HI-RES	WIND ONLY
RESOLUTION (s °)	nomally 50 km	50 km	25 km	Egg: 25x35 km Slice: 6x25km	25/50 km
SWATH, km	 ~750 ~750	 500	 600 600	 1400, 1800	 500 500
INCIDENCE ANGLES	0° - 70°	18° - 59°	17° - 60°	46° & 54.4°	25° - 65°
DAILY COVERAGE	VARIABLE	< 41 %	78 %	92 %	65 %
MISSION & DATES	SEASAT: 6/78 ÷ 10/78	ERS-1: 92Ð96 ERS-2: 95Ð01	ADEOS-I: 8/96 ÷ 6/97	QuikSCAT: 6/99- ADEOS-II: 1/02-10/02	METOP: 6/2007-

Figure 6.14: Spaceborne wind scatterometer comparison.

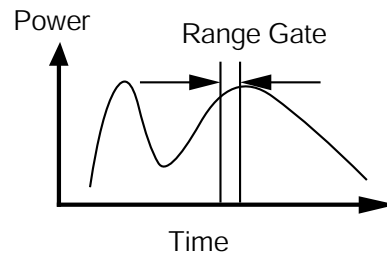


Figure 6.15: Diagram of the power versus time for an echo signal illustrating range gating.

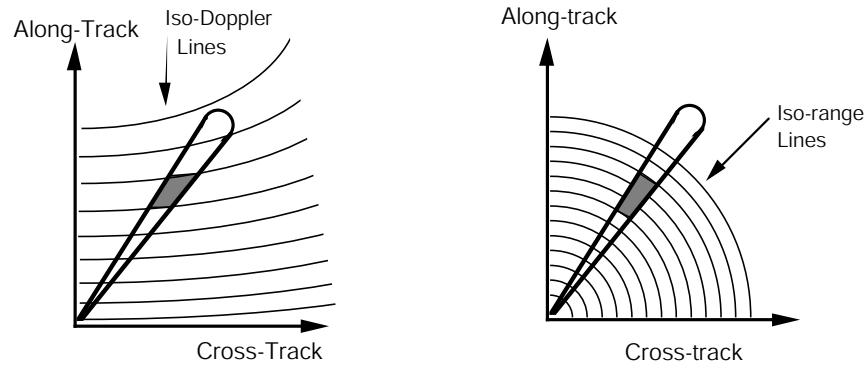


Figure 6.16: Methods for along-beam resolution for a long, thin antenna pattern. (left) Iso-Doppler filtering. (right) Range gating or range compression.

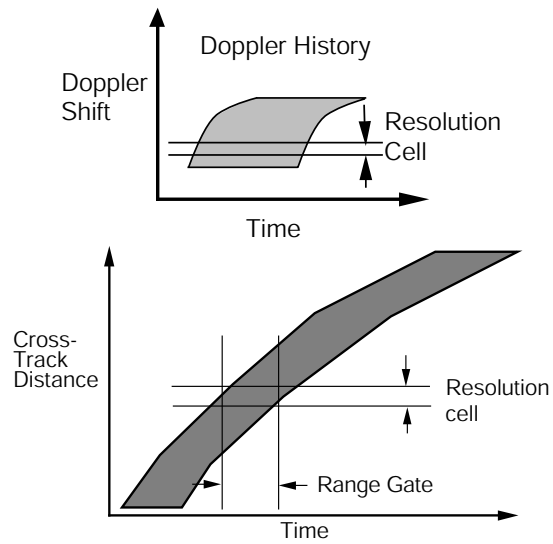


Figure 6.17: Diagram of the time/Doppler history of (left) a long-pulse echo signal and (right) a short-pulse echo signal for a forward-facting fan-beam antenna. The gray area indicates the region of Doppler shift and time delay present in the echo.

gating as also illustrated in Fig. 6.16. In this case, a short pulse is used. The time of flight of the pulse corresponds to the range and by selecting a narrow range of time-of-flights (a narrow range gate), an along-beam resolution element is defined. Figure 6.16 illustrates the relationship between the time-of-flight and along-beam distance. We note that this approach can be used even for antennas aligned perpendicular to the flight track. Also, longer pulses can be used with range compression to achieve finer time resolution (see later discussion under SAR range resolution).

Both the Doppler and isorange approaches define, in effect, cross-track resolution elements which cover a wide swath to the side of the flight path (see Fig. 6.18). By selecting the appropriate range gate timing and/or Doppler filter bandwidth, cross-track aligned resolution elements are defined for the forward and aft-facing antennas that enable multi-azimuth observation of the same location on the Earth as the spacecraft passes over the site (Naderi et al., 1991).

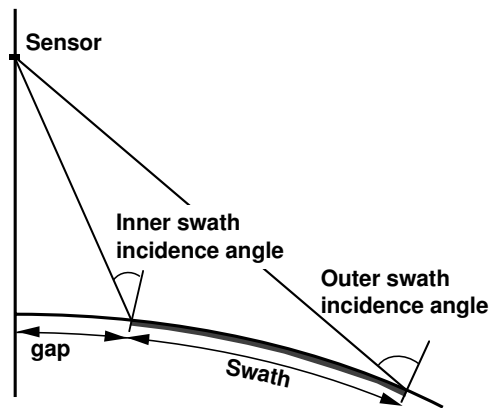


Figure 6.18: Side-looking radar swath for a wideswath radar. Note the variation in incidence angles over the swath. The azimuth angle may be tilted forward, aft or be orthogonal to the flight path. It is generally orthogonal for SAR systems.

Note that, unlike a radiometer and the helically scanning SeaWinds scatterometer, a fan-beam scatterometer measures σ^o at a variety of different incidence angles, see Fig. 6.18. Since the target response is different at different incidence angles, one must be extremely careful when combining measurements taken at different incidence angles. A solution to this problem is to use a model for the target response (such as the geophysical model function used for wind retrieval over the ocean). Over most natural surfaces in the incidence angle range $20^\circ \leq \theta \leq 60^\circ$, corresponding to the range of scatterometer measurements, a well known approximate

model expresses σ° (in dB) as a linear function of incidence angle, i.e.

$$\sigma_{\text{dB}}^\circ(\theta) = \mathcal{A} + \mathcal{B}(\theta - 40^\circ) \quad (6.15)$$

where \mathcal{A} is the 40° incidence angle-normalized σ° and \mathcal{B} is the dependence of σ° on the incidence angle θ . The \mathcal{A} and \mathcal{B} coefficients are functions of the geophysical properties of the surface. Note that 40° is the approximate center incidence angle over the swath and is a convenient angle for making comparative analyses¹.

6.4.4 Side-Looking Airborne Radar

Side-looking airborne radar (SLAR) is an imaging radar based on real-aperture techniques (Ulaby et al., 1981). Using a narrow fan-beam antenna and range compression, radar backscatter images can be generated. Range resolution is defined by the pulse compress, while azimuth resolution is dictated by the azimuth beam width of the antenna illumination pattern. To further improve the azimuth resolution, synthetic aperture techniques are used. Due to the low resolution of SLAR when used from space, few SLAR systems have been orbited. The Russian Okean and Almaz sensors are the exceptions.

6.4.5 Synthetic Aperture Radar

Synthetic Aperture Radar (SAR) has its origins in SLAR but has improved azimuth resolution due to the use of Doppler information in the return echo. This technique was originally called Doppler beam sharpening, but is known today as synthetic aperture radar. SAR theory is covered in extensive detail in a number of sources, e.g. (Curlander and McDonough, 1991; Elachi, 1988; Henderson and Lewis, 1998; Franschetti and Lanari, 1999). The general goal of SAR is to provide radar images of the surface (Leberl, 1990; Oliver and Quegan, 1990).

The most common form of SAR used in remote sensing is strip-map SAR, which generates a long strip-map image. A brief introduction to strip-map SAR is given in the following. Spotlight mode SAR differs in that the antenna is pointed, or steered, toward the target area as the platform moves past (Jakowatz et al., 1996). ScanSAR is closely related to strip-map SAR, but rapidly switches between multiple antenna beams to increase the swath width.

As a radar moves past the target transmitting pulses, each of the echoes from the target have a different frequency shift due to the relative velocity of the platform and the surface. This can be explained as due to the Doppler effect (hence, the

¹While not applicable for all targets, over the Amazon Rainforest (which exhibits high volume scattering) a “gamma” normalization may be used with some success, i.e., $\gamma(k) = \sigma^\circ(k) / \cos \theta(k)$ where $\theta(k)$ is the incidence angle of the k^{th} measurement of σ° . Over the incidence angle range $[20^\circ, 60^\circ]$, $\gamma(k)$ is approximately constant, i.e., not a function of incidence angle.

original description, Doppler sharpening), but is better explained as being due to the change in phase of the signal due to the changing range to the target. Range resolution is typically obtained using pulse compression and matched filtering. Using matched filtering of the pulses in the along-track direction to select the phase history of the target generates azimuth resolution, effectively narrowing the azimuth beamwidth. This azimuth matched filter processing is equivalent to synthesis of an array antenna in the motion direction where each element of the synthetic array corresponds to the actual antenna at the locations of the received pulses.

An approximation of the azimuth resolution for synthetic aperture radar can be estimated using the idea of a synthetic array antenna. As shown in (Elachi, 1988), a radar with an azimuth antenna of length L_{az} moving at a constant velocity, the length of the synthetic array is equivalent to the size of the beam footprint on the ground. The size of the synthetic array is given as

$$L_s = \frac{2\lambda h}{L_{az}} \quad (6.16)$$

where L_{az} is the azimuth size of the antenna and h is the height of the platform. The new $3dB$ azimuth beamwidth of the synthesized array is

$$\theta_{SAR} \approx \frac{\lambda}{L_s} = \frac{L_{az}}{2h}. \quad (6.17)$$

The corresponding azimuth synthesized resolution is given by

$$\delta_{SAR} \approx h\theta_{SAR} = \frac{L_{az}}{2}. \quad (6.18)$$

From this we note that the effective resolution of a SAR image is independent of the platform height.

While synthetic aperture radar provides a large improvement in azimuth resolution over real aperture radar, it requires coherent radar hardware to preserve signal phase, storage of the received echos, and complicated computer processing to produce an image.

SARs have been used in a variety of applications, from vegetation monitoring to ocean sensing (Elachi, 1988; Elachi et al., 1984; Jackson and Apel, 2004).

6.4.5.1 Interferometric SAR

Unlike optical sensors, SAR is a coherent (phase preserving) technique which measures range. Preservation of the signal phase can be exploited to provide topographic information using interferometric techniques (Hanssen, 2001; Henderson and Lewis, 1998; Madsen et al., 1993). An interferometric SAR uses two antennas at different positions to infer scene topography. While most interferometric SAR

systems do this simultaneously, interferometric processing of multiple spaceborne SAR passes over a scene has been demonstrated (see, for example, (Henderson and Lewis, 1998)).

As seen from Fig. 6.19, when two SAR range observations, r_a and r_b , from different positions are available, basic trigonometry enables estimation of the height of the target relative to a reference.

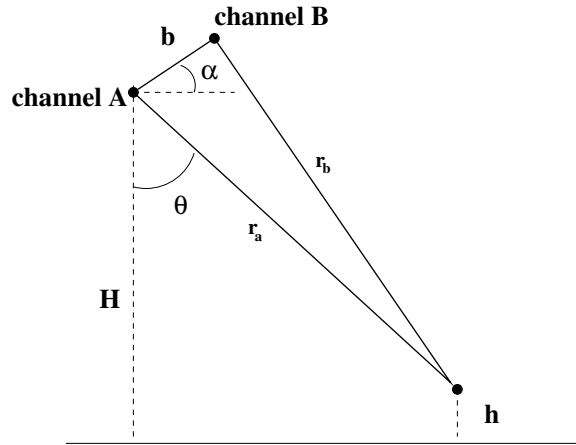


Figure 6.19: Interferometric SAR geometry model.

The height of the target can be found using the law of cosines (Franschetti and Lanari, 1999),

$$r_b^2 = r_a^2 + b^2 - 2br_a \sin(\theta - \alpha). \quad (6.19)$$

The target height, h , is then found by the equation

$$h = H - r_a \cos(\theta). \quad (6.20)$$

Typically, one of the ranges, the length of the baseline, and the height, H , are known exactly. This implies that the accuracy of the target height estimate, h , is dependent upon the measurement of the second range, r_a , or upon the change in range, Δr , which is defined as

$$\Delta r = r_b - r_a. \quad (6.21)$$

Graham (Franschetti and Lanari, 1999) first proposed the idea of using the phase difference from two SAR images, slightly offset, to determine the value of Δr . The

idea is that if one of the received SAR images has a signal given by

$$\gamma_1 = A_1 \exp\left(-j \frac{4\pi}{\lambda} r_a\right) \quad (6.22)$$

and a second SAR image, which is slightly offset from the first, has a signal of

$$\gamma_2 = A_2 \exp\left(-j \frac{4\pi}{\lambda} r_b\right), \quad (6.23)$$

then the phase difference

$$\Delta\phi = \arg[(\gamma_1)(\gamma_2)^*] = \frac{4\pi}{\lambda} \Delta r \quad (6.24)$$

enables estimation of the range difference, Δr . The accuracy of the estimate is related to the size of the wavelength and the size of the baseline, b . Two collocated single-look complex (SLC) SAR images, one from each channel, are used to make a phase difference image known as an interferogram. The phase differences contained in interferograms are initially wrapped between 0 and 2π and require two-dimensional phase unwrapping in order to find the Δr estimate (Curlander and Mcdonough, 1991). Once the unwrapped phase is computed, the height is computed, the phase that would be due to a “flat-earth” is computed and removed from the interferogram. When a high quality digital elevation map (DEM) is available, the “flat-earth” phase may be replaced with the DEM phase. The topography relative to a “flat-earth” reference is then computed from the residual phase (Madsen et al., 1993).

Interferometry has found many applications including high-resolution digital elevation map (DEM) creation (Madsen et al., 1993) and differential images using multiple interferograms (Reigber and Scheiber, 2003). Along-track interferometry can be used to extract current velocity on the ocean’s surface, as well as ground moving targets.

6.4.5.2 Polarimetric SAR

Polarimetric SAR is a relatively recent development (Ulaby et al., 1990). In polarimetric SAR, multiple combinations of transmit and receive polarization (and the phase relationship between the polarizations) are used to create SAR imagery. The additional images provide more information about the surface and in particular provide additional information about the number of bounces in the scattered signal (Elachi and Ulaby, 2000). This improves surface characterization.

6.4.6 Airborne Radar Systems

Aircraft were the first platforms widely used for microwave remote sensing. Altimeters are standard equipment on aircraft and are used for measuring the height

of the aircraft over the ground. Altimeters used for remote sensing have been primarily used over the ocean and the polar regions of the earth.

A number of scatterometers and SARs have been operated from aircraft both for research and surveillance. The list is too long to consider here. SAR and side-looking real-aperture radars are commonly used on military aircraft; however, these are not generally available as mapping data sets.

NASA's Jet Propulsion Laboratory has developed a number of airborne SAR systems including AIRSAR, POLSAR, TOPSAR, and others which have been extensively used in studies (Rodriguez and Martin, 1991; Zebker and Goldstein, 1986). Many other organizations have developed airborne SAR systems, including ERIM, Donier, etc.

6.4.7 Spaceborne Radar Systems

With their larger power requirements to support an active transmitter, fewer earth-observing radar remote sensing systems have flown than radiometer systems. However, many spaceborne radar systems have flown and are currently operating. The next section provides a brief summary of significant microwave radar remote sensing systems.

6.5 Spaceborne Radar Systems

The goal of this section is to summarize basic sensor information about important Earth-observing radar which have operated aboard spacecraft. Historical sensors are considered first, followed by contemporary (recent and currently operating sensors) and then planned sensors. Within each category, the main classes of active sensors (altimeters, scatterometers, SARs, and weather radars) are separately considered in sequence.

6.5.1 Historical Radar Sensors

The landmark Seasat satellite launched in 1978 incorporated each of the major microwave sensor classes, including a radiometer (SMMR), an altimeter, a scatterometer (SASS) and a SAR. Some of these (notably the active sensors) represent the first of this class of sensor to fly in space (Fu and Holt, 1982; Gloersen and Barath, 1977; Grantham et al., 1977; Njoku et al., 1980). In this section we consider these and other historical active sensors.

6.5.1.1 Historic Altimeters

Spaceborne altimetry has a long history of ocean measurements. Selected historic altimeters are described in this section.

6.5.1.1.1 *GEOS-3* - The GEOS-3 altimeter flew in 1974 (Martin and Kolenkiewicz, 1981). This research mission was designed to determine the feasibility of spaceborne altimeters to map sea surface topography and map the geod.

Table 6.19: Sensor characteristics for the GEOS-3 Altimeter.

Sensor	GEOS-3 Altimeter
Sensor Type	altimeter
Sensor Scan	nadir
Polarization	N/A
Center Frequency	Ku-band 13.9 GHz
Operating Bandwidth	80 MHz
Pulse Length	12 or 200 ns
PRF	100 Hz
Fundamental Measurement	time-of-flight (s)
Fundamental Resolution	pulse-limited, footprint
Coverage	global oceans, 60N to 63S
Footprint Shape	circular
Incidence Angle	0°
Mission Length	1975 - 1978
Spacecraft	GEOS-3
Orbit	818 k by 858 km 115° inclination angle
Key Products	sea-level height significant wave height wind speed
Product Resolution	50 cm
Product Accuracy	topography: 50 cm significant wave height: 25%
Data Availability	podaac.jpl.nasa.gov

6.5.1.1.2 *SeaSat Radar Altimeter (ALT)* - Part of the landmark Seasat-1 mission, the Seasat radar altimeter (ALT) was designed to measure wave height and the distance between the spacecraft and the ocean surface. When combined with accurate orbit determination, precise maps of sea surface topography were produced. Greenland ice sheet topography was also estimated (Martin et al., 1983). Over the ocean, the height accuracy was estimated to be within ± 10 cm (Townsend, 1980). ALT operated for 3 months in 1978 and set the stage for follow-on missions.

Table 6.20: Sensor characteristics for the Seasat Radar Altimeter.

Sensor	Seasat Radar Altimeter
Sensor Type	altimeter
Sensor Scan	nadir
Polarization	N/A
Center Frequency	Ku-band 13.56 GHz
Operating Bandwidth	312.5 kHz
Transmit power	2 kW peak
Fundamental Measurement	time-of-flight (s) radar backscatter (σ^0)
Fundamental Resolution	pulse-limited, footprint
Coverage	global oceans, 60N to 63S
Swath Width	2.4 to 12 km
Footprint Shape	circular ring
Footprint Size	2.4 to 12 km
Incidence Angle	variable, 0°
Mission Length	7 Jul. 1978 - 10 Oct. 1978
Spacecraft	Seasat-1
Orbit	790 km sun-synchronous 108° inclination angle near-circular
Key Products	sea-level height significant wave height wind speed
Product Resolution	10 cm
Product Accuracy	topography: 10 cm significant wave height: 0.5 m or 10% σ^0 : 1 dB
Product Range	0 to 20 m
Data Availability	podaac.jpl.nasa.gov

6.5.1.1.3 TOPEX/Poseidon - The joint U.S.-French TOPEX/Poseidon mission was launched on 10 Aug. 1992 (Fu et al., 1994). The spacecraft carried a dual-frequency (C- and Ku-band) altimeter, a second single frequency (Ku-band) altimeter, and a nadir looking microwave radiometer to measure water vapor (Fu et al., 1994). Designed to measure sea-level accuracy to better than 4.2 cm, it provides coverages from 66° N to 66° S. The orbit was carefully chosen to minimize the effects of tidal aliasing so as to minimize measurement error.

Table 6.21: Sensor characteristics for the Topex/Poseidon Altimeter.

Sensor	Topex/Poseidon Altimeters
Sensor Type	altimeter
Sensor Scan	nadir
Polarization	N/A
Center Frequency	C-band: 5.3 GHz, Ku-band: 13.6 GHz
Operating Bandwidth	320 MHz
Fundamental Measurement	time-of-flight (s) radar backscatter (σ^0)
Fundamental Resolution	pulse-limited footprint
Swath Width	(nadir viewing)
Footprint Shape	circular
Incidence Angle	0°
Mission Length	1996-2006
Spacecraft	TOPEX
Orbit	1336 km non-sun-synchronous circular 66° inclination angle 10 day repeat cycle
Key Products	sea-level height significant wave height wind speed
Product Resolution	3 cm
Product Accuracy	topography: 10 cm significant wave height: 13 cm σ^0 : 1 dB
Data Availability	podaac.jpl.nasa.gov

6.5.1.1.4 *Geosat* - Geosat was a unique gravity-gradient stabilized spacecraft designed to carry a radar altimeter (MacArthur et al., 1971) for the U.S. NAVY. The Geosat altimeter is essentially a copy of the Seasat altimeter. Geosat operated for three years.

Table 6.22: Sensor characteristics for the Geosat Altimeter.

Sensor	Geosat Altimeter
Sensor Type	altimeter
Sensor Scan	nadir
Polarization	N/A
Center Frequency	13.50 GHz
Operating Bandwidth	320 MHz
Transmit power	20 W
Antenna beamwidth	2°
Fundamental Measurement	time-of-flight (s) radar backscatter (σ^0)
Fundamental Resolution	pulse-limited footprint
Footprint Shape	circular
Incidence Angle	0°
Mission Length	1986-1990
Spacecraft	Geosat
Orbit	760 km by 817 km 108.05° inclination angle 17 day repeat cycle
Key Products	sea-level height significant wave height wind speed
Product Resolution	10 cm
Product Accuracy	topography: 10 cm significant wave height: 0.5 m or 10% σ^0 : 1 dB
Data Availability	www.nodc.noaa.gov www.nsidc.org

6.5.1.1.5 *ERS-1/2 Altimeter* - The European Earth Resources Satellite (ERS) -1 and -2 included an altimeter, though the data utility is somewhat limited by the fact that the sun-synchronous orbit results in aliasing of the ocean tidal signature, which has the effect of reducing the accuracy of the height measurements (Sandwell, 1990).

Table 6.23: Sensor characteristics for the ERS-1 Altimeter.

Sensor	ERS-1 Altimeter
Sensor Type	altimeter
Sensor Scan	nadir
Polarization	N/A
Center Frequency	Ku-band 13.8 GHz
Operating Bandwidth	400 MHz
Fundamental Measurement	time-of-flight (s) radar backscatter (σ^0)
Fundamental Resolution	pulse limited, footprint
Footprint Shape	circular
Incidence Angle	variable, 0°
Mission Length	ERS-1: 1991-1996 ERS-2: 1995-
Spacecraft	ERS-1/ERS-2
Orbit	780 km sun-synchronous 98.5° inclination angle
Key Products	sea-level height significant wave height wind speed
Product Resolution	10 cm
Product Accuracy	topography: 10 cm significant wave height: 13 cm
Data Availability	podaac.jpl.nasa.gov

6.5.1.2 Historic Scatterometers

Scatterometry began with an experiment on a manned mission, which demonstrated its utility for land and ocean observation. Since then, several types of scatterometers have flown in space. Selected historic scatterometers are described in this section.

6.5.1.2.1 Skylab S-193 - The Skylab S-193 altimeter/scatterometer was the first spaceborne radar scatterometer and was flown as a demonstration experiment (Young, 1976). It was used to study the Ku-band radar signature of the land and ocean. S-193 measurements, coupled with aircraft observations, suggested that near-surface winds could be measured from space and lead to the development of all subsequent wind scatterometers.

Table 6.24: Sensor characteristics for the Skylab S-193 Scatterometer.

Sensor	Skylab S-193 Scatterometer
Sensor Type	scatterometer
Sensor Scan	pencil-beam
Polarization	HH, VV
Center Frequency	14.6 GHz
Transmit power	100 W
Fundamental Measurement	radar backscatter (σ^0)
Fundamental Resolution	footprint
Coverage	spot
Swath Width	N/A
Footprint Shape	elliptical
Footprint Size	incidence angle dependent
Incidence Angle	variable
Spacecraft	Skylab
Key Products	radar backscatter
Data Availability	(unknown)

6.5.1.2.2 *Seasat Scatterometer (SASS)* - SASS was the first spaceborne wind scatterometer (Grantham et al., 1977; Grantham, 1982; Johnson et al., 1980). It operated for 3 months in 1978, collecting Ku-band σ^o data at nominally 50 km resolution over a variable and irregular swath. SASS used 4 dual-pol fan-beam antennas to provide along-track resolution and fixed frequency Doppler filters to provide along-track resolution. Designed for wind observations, SASS could be operated in a variety of modes to experiment with the optimal polarization mix. Unfortunately, the fixed frequency Doppler filters employed limited the fore/aft coregistration of the backscatter measurements. SASS provided an extensive global data set of Ku-band backscatter measurements (Kennett and Li, 1989; Long and Drinkwater, 1994; Long et al., 2001) and led to a number of follow-on missions, including NSCAT (Naderi et al., 1991) and SeaWinds. In addition to pre-launch calibration, post-launch calibration was conducted using distributed earth targets such as the Amazon forest (Birrer et al., 1982; Long and Skouson, 1996). The SASS antenna measurement geometry is illustrated in Fig. 6.20. Along-beam resolution is provided by Doppler filtering, see Fig 6.21.

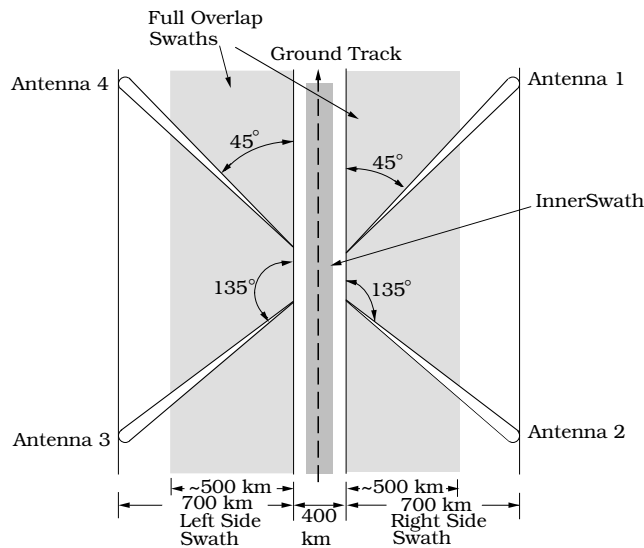


Figure 6.20: Illustration of the SASS measurement geometry showing the 3dB antenna illumination footprints. Doppler filtering resolves the footprints into smaller segments known as “cells”. Grey region indicates portions of swath for which the forward and aft-looking measurements overlap.

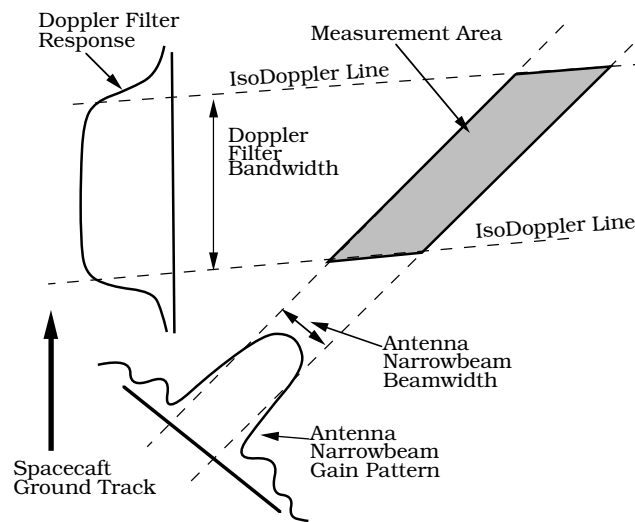


Figure 6.21: Illustration of the SASS and NSCAT resolution element (cell) measurement geometry which is based on Doppler filtering and the antenna illumination pattern.

Table 6.25: Sensor characteristics for SASS.

Sensor	Seasat Scatterometer (SASS)
Sensor Type	fixed Doppler, scatterometer
Sensor Scan	fan-beam, 4 beams, dual-sided
Polarization	VV, HH
Center Frequency	14.6 GHz
Operating Bandwidth	CW
Transmit power	110 W
Pulse Length	5 ms
Fundamental Measurement	radar backscatter (σ^0)
Fundamental Resolution	footprint
Radiometric Accuracy (K_p)	0.05
Radiometric Stability ($\pm\sigma^0$)	0.15 dB
Coverage	global
Swath Width	500 km
Footprint Shape	fan-beam
Footprint Size	variable
Incidence Angle	variable, 0° – 70°
Mission Length	1978
Spacecraft	Seasat
Orbit	805 km sun-synchronous
Key Products	ocean winds radar backscatter
Product Resolution	50 km
Product Accuracy	2 m/s, 20°
Product Range	0-35 m/s
Data Availability	winds and backscatter : podaac.jpl.nasa.gov backscatter images : www.scp.byu.edu

6.5.1.2.3 *NASA Scatterometer (NSCAT)* - Designed to measure near-surface winds over the ocean, NSCAT was a follow-on to SASS (Naderi et al., 1991) and used a digital Doppler processor rather than fixed analog filters (Long et al., 1988). The digital processor ensured a fixed-width swath with better fore/aft measurement coregistration (Naderi et al., 1991). NSCAT included an additional antenna over SASS and provided 25 km resolution measurements on a regular 25 km grid. It operated for nine months before the spacecraft power system failed in June 1996. Like SASS, NSCAT post-launch calibration was conducted using distributed earth targets such as the Amazon forest (Tsai et al., 1999; Zec et al., 1999). NSCAT backscatter data has been widely used in studies of land and ice, e.g., (Long et al., 2001; Long and Drinkwater, 1999). The NSCAT measurement geometry is illustrated in Figs. 6.22 and 6.21.

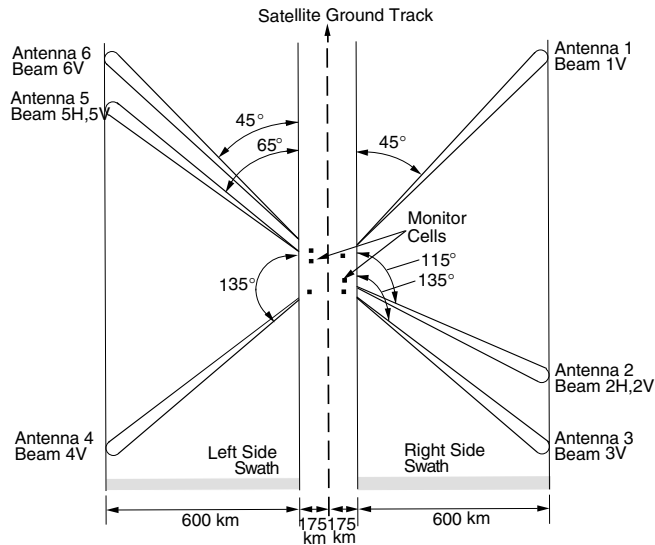


Figure 6.22: Illustration of the NSCAT measurement geometry showing the 3dB antenna illumination footprints. Doppler filtering resolves the footprints into smaller segments known as “cells”.

Table 6.26: Sensor characteristics for NSCAT.

Sensor	NASA Scatterometer (NSCAT)
Sensor Type	variable Doppler scatterometer
Sensor Scan	fan-beam, 6 beams, dual-sided
Polarization	VV, HH
Center Frequency	13.995 GHz
Operating Bandwidth	ICW
Transmit power	110 W
Pulse Length	5 ms
PRF	62 Hz
Fundamental Measurement	radar backscatter (σ^0)
Fundamental Resolution	footprint
Radiometric Accuracy (K_p)	0.02-0.07
Radiometric Stability ($\pm\sigma^0$)	0.1 dB
Coverage	global, 2 days
Swath Width	two 600 km swaths with 700 km gap
Footprint Shape	fan-beam
Footprint Size	5×950 km
Incidence Angle	variable, 17° – 60°
Mission Length	1996-97
Spacecraft	ADEOS-I (Midori-I)
Orbit	955 km sun-synchronous, 10 a.m.
Key Products	ocean winds radar backscatter
Product Resolution	25 km, 50 km
Product Accuracy	2 m/s, 20°
Product Range	0-50 m/s
Data Availability	winds and backscatter : podaac.jpl.nasa.gov backscatter images : www.scp.byu.edu

6.5.1.2.4 *ERS AMI Scatterometer Mode* - The European Remote Sensing (ERS) ERS-1 and ERS-2 Advanced Microwave Instrument (AMI) in scatterometer mode uses multiple fan-beam antennas to make σ^o measurements at different azimuth angles over a wide swath (Attema, 1991). Each antenna produces an instantaneous footprint several hundred kilometers long and a few kilometers wide. The antennas were arranged at three azimuth angles and sweep out a nominally 500 km wide swath. This swath is resolved into smaller cells using pulse timing and range gate filtering as described below. Nominally 50 km resolution σ^o measurements are reported on 25 km centers for each antenna. The along-track timing is complicated by the synthetic aperture radar (SAR) wave mode which time shares the transmitter. Unfortunately, scatterometer data cannot be collected during SAR operations.

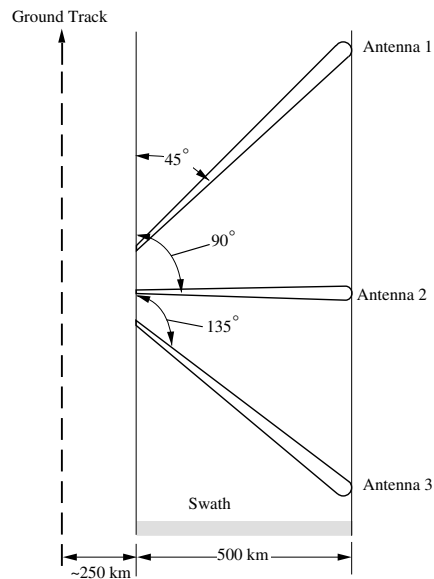


Figure 6.23: Illustration of the ERS-1/2 AMI scatterometer mode (ESCAT) measurement geometry showing the 3dB antenna illumination footprints. Range gate filtering resolves the footprints into smaller areas.

The ERS-1/2 AMI digitizes the received echos and telemeters the data to the ground for further processing. On the ground, the pulses corresponding to each along-track cell are integrated. Range gating is separately applied to each echo to achieve cross-track resolution and the power computed. The pulses corresponding to each along-track cell are then integrated into a single “50 km” resolution measurement. A 25 km spacing grid of nominally 50 km σ^o measurements are obtained

from each antenna. While not precisely defined in the available literature, a spatial smoothing filter is applied when integrating the pulses. For each grid element there are three measurements of σ^o , one from each antenna beam. In many land and ice applications these may be combined; however, care must be used for surfaces exhibiting azimuthal variation in σ^o (notably the ocean) (Early and Long, 1997). The ERS scatterometer measurement geometry is illustrated in Figs. 6.23 and 6.24. Due to spacecraft attitude system failure, the ERS-2 scatterometer ceased global coverage in 2001, though limited coverage is available through 2008.

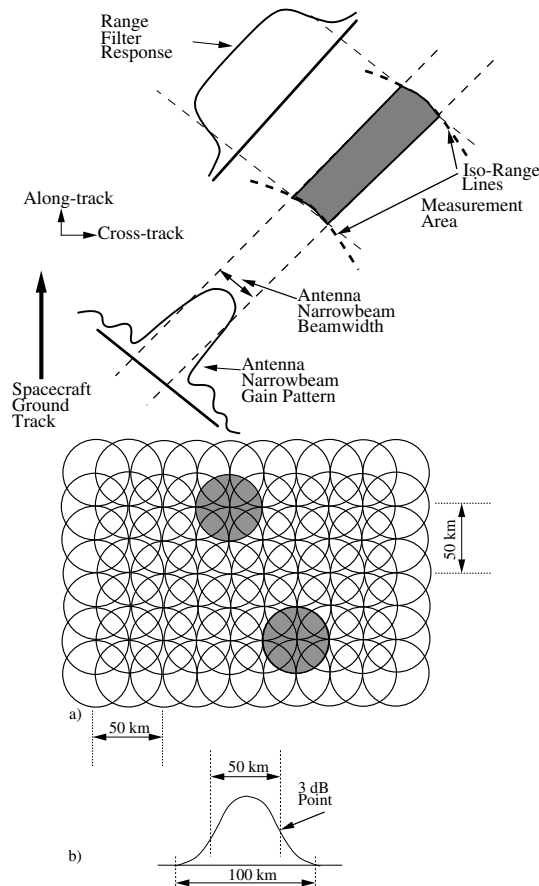


Figure 6.24: (top) ERS-1/2 scatterometer mode measurement geometry. Resolution is based on range-filtering. (bottom) ERS-1/2 scatterometer mode σ^o geometry. Multiple pulse measurements are averaged into (a) 50 km measurements on a 25 km grid weight with (b) a Hamming window.

Table 6.27: Sensor characteristics for the ERS-1/2 AMI Scatterometer Mode.

Sensor	ERS-1/2 AMI Scatterometer Mode
Sensor Type	range-gate, scatterometer
Sensor Scan	fan-beam, 3-beams, single sided
Polarization	VV
Center Frequency	5.3 GHz
Pulse Length	70-135 μ s
PRF	\sim 127 Hz
Operating Bandwidth	\sim 15 kHz
Transmit power	5 kW
Fundamental Measurement	radar backscatter (σ^o)
Fundamental Resolution	footprint
Radiometric Accuracy (K_p)	0.05
Radiometric Stability ($\pm\sigma^o$)	0.57 dB
Coverage	global
Swath Width	500 km
Footprint Shape	fan-beam, averaged
Footprint Size	5 \times 750 km
Incidence Angle	variable, 18 $^\circ$ –69 $^\circ$
Mission Length	ERS-1: 1992-96 ERS-2: 1996-
Spacecraft	ERS
Orbit	780 km sun-synchronous 98.5 $^\circ$ inclination angle
Key Products	ocean winds radar backscatter
Product Resolution	50 km, 25 km posting
Product Accuracy	4-24 m/s: 2 m/s or 10%, 20 $^\circ$
Product Range	0-35 m/s
Data Availability	winds and backscatter : www.ifremer.org backscatter images : www.scp.byu.edu

6.5.1.3 Historic SARs

Given their large power requirements and high data rates, a surprising number of SAR systems have flown in space with several on the U.S. Space Shuttle program. Selected historic SAR sensors are described in this section. Because of the complexity of the sensors and their coverage swaths, only very brief summaries of the sensors are provided. Readers seeking additional information are referred to cited references and data distribution sites.

6.5.1.3.1 Seasat SAR - The Seasat SAR provides the first synoptic, high-resolution SAR images of the Earth's surface (Fu and Holt, 1982; Jordan, 1980). It operated for 99 days in 1978. Data was collected only when the spacecraft was in view of a ground station which limited coverage to areas around Goldstone, California; Fairbanks, Alaska; Merritt Island, Florida; Shoe Cove, Newfoundland, Canada; and Oakhanger, United Kingdom. Originally, SAR processing was done optically, but eventually the entire archive was digitally processed. Approximately 500 passes of 5 min each were collected.

Table 6.28: Sensor characteristics for the Seasat SAR.

Sensor	Seasat SAR
Sensor Type	SAR
Sensor Scan	fan-beam, SAR
Polarization	HH
Center Frequency	1.275 GHz
Pulse Length	33.4 μ s
PRF	1463-1640
Operating Bandwidth	19 MHz
Transmit power	1 kW
Fundamental Measurement	radar backscatter (σ^o)
Coverage	limited to near ground stations
Swath Width	100 km
Incidence Angle	variable, 20°–26°
Mission Length	99 days, 1978
Spacecraft	Seasat-A
Orbit	800 km circular sun-synchronous 108° inclination angle
Key Products	radar backscatter images
Product Resolution	<i>sim</i> 25 m
Data Availability	southport.jpl.nasa.gov/scienceapps/seasat.html

6.5.1.3.2 Shuttle Imaging Radar A (SIR-A) - SIR-A was the first of the NASA/JPL shuttle radar series and was essentially a duplicate of the Seasat SAR. It was launched on Nov. 12, 1984 aboard the Space Shuttle Columbia and used a fixed look angle. Data was collected over a several day period.

Table 6.29: Sensor characteristics for SIR-A.

Sensor	SIR-A
Sensor Type	SAR
Sensor Scan	fan-beam, SAR
Polarization	HH
Center Frequency	1.275 GHz
Pulse Length	30.4 μ s
PRF	1464-1824 Hz
Operating Bandwidth	6 MHz
Transmit power	1 kW
Fundamental Measurement	radar backscatter (σ^0)
Coverage	near-global
Swath Width	variable, 50 km
Incidence Angle	variable, 47°–53°
Mission Length	few days in 1984
Spacecraft	Space Shuttle (STS-2)
Orbit	222 km \times 231 km near circular 38° inclination angle 37 orbits (3 days)
Key Products	radar backscatter images
Product Resolution	40 m \times 40 m
Data Availability	southport.jpl.nasa.gov

6.5.1.3.3 *Shuttle Imaging Radar B (SIR-B)* - SIR-B was the second in the NASA/JPL shuttle radar series (Cimino et al., 1986). It was launched on October 5, 1984 aboard the Space Shuttle Challenger on flight 41-G into a nominally circular orbit. Like SIR-A it used a fixed look angle and operated from the U.S. space shuttle. However, the shuttle altitude was varied during the mission to enable multiple incidence angle observations of the same location. Data was recorded on-board the space shuttle using a film recorder for later processing but has not been made widely available.

Table 6.30: Sensor characteristics for SIR-B.

Sensor	SIR-B
Sensor Type	SAR
Sensor Scan	fan-beam, SAR
Polarization	HH
Center Frequency	1.275 GHz
Pulse Length	30.4 μ s
Operating Bandwidth	12 MHz
Transmit power	1.12 kW
Fundamental Measurement	radar backscatter (σ^0)
Coverage	limited near-global
Swath Width	variable, 20-40 km
Incidence Angle	variable, 15°–65°
Mission Length	few days in 1984
Spacecraft	Space Shuttle (STS-41G)
Orbit	360, 257, 224 km circular 57° <i>irc</i> inclination angle
Key Products	radar backscatter images
Product Resolution	20-40 m \times 16-58 m

6.5.1.3.4 *Spaceborne Imaging Radar-C/X-band Synthetic Aperture Radar (SIR-C/X-SAR)* - SIR-C/X-SAR was a joint project of the National Aeronautics and Space Administration (NASA), the German Space Agency (DARA) and the Italian Space Agency (ASI) (Evans et al., 1997; Jordan et al., 1991; Stofan et al., 1995). The multipolarization SIR-C SAR operated at L-Band and C-Band while X-SAR operated at X-band. The SIR-C/XSAR system was flown twice aboard the U.S. Space Shuttle in 1994, STA-59 9 to 20 April and STS-68 30 September to 11 October 1994. The shuttle flew in 225 km in a circular, 57° inclination orbit. SIR-C used an active phased array antenna which could be electronically steered. X-SAR was mechanically tilted. Data was recorded on-board the space shuttle for ground processing.

Table 6.31: Sensor characteristics for SIR-C/X-SAR.

Sensor	SIR-C/X-SAR
Sensor Type	SAR
Sensor Scan	fan-beam, SAR
Polarization	SIR-C: HH, VV, VH, HV X-SAR: VV
Center Frequency	SIR-C: 1.275 and 5.17 GHz X-SAR: 9.67 GHz
Pulse Length	SIR-C: 33.8, 16.9, 8.5 us X-SAR: 40 us
PRF	1395-1736
Operating Bandwidth	10, 20, and 40 MHz
Transmit power	SIR-C: 1.275 GHz: 4400 W 5.17 GHz: 1200 W X-SAR: 1400 W
Fundamental Measurement	radar backscatter (σ^0)
Radiometric Stability ($\pm\sigma^0$)	SIR-C: 1.5 dB & X-SAR: 2.5 dB
Coverage	limited coverage, near-global
Swath Width	15 km to 90 km, variable
Incidence Angle	variable, 17° – 63°
Mission Length	two 11 day missions in 1994
Spacecraft	Space Shuttle STS-59 & STS-68
Orbit	nominally 225 km circular
Key Products	radar backscatter images some interferometric images
Product Resolution	~ 30 m
Data Availability	southport.jpl.nasa.gov www.asf.alaska.edu

6.5.1.3.5 Shuttle Radar Topography Mission (SRTM) - Using modified SIR-C/X-SAR hardware to support interferometric operation, SRTM became the first spaceborne single-pass interferometer. It obtained global elevation data to create the most complete (80% of the Earth's surface) high-resolution digital topographic database of Earth ever made (Farr et al., 2007; Moreira et al., 1995; Coltelli et al., 1996). SRTM flew onboard the Space Shuttle Endeavour during an 11-day mission in February of 2000. The data set has become an important one in earth studies.

A second antenna system was added to the SIR-C/X-SAR system to enable single pass cross-track interferometric measurements. The "outboard" antennas extended 60 m from the main antenna in the shuttle bay in order to form the interferometric SAR baseline for the C- and X-band channels. The L-band channel of SIR-C was not used for SRTM. SRTM extracted topographic information from the SAR data on a 30 m grid. The estimated vertical accuracy is 16 m.

Table 6.32: Sensor characteristics for SRTM.

Sensor	SRTM (modified SIR-C/X-SAR)
Sensor Type	interferometric SAR
Sensor Scan	dual antenna fan-beam, SAR
Polarization	SIR-C: HH, VV, VH, HV X-SAR: VV
Center Frequency	SIR-C: 5.17 GHz X-SAR: 9.67 GHz
Pulse Length	SIR-C: 33.8, 16.9, 8.5 us X-SAR: 40 us
PRF	1395-1736
Operating Bandwidth	10, 20, and 40 MHz
Transmit power	SIR-C 5.17 GHz: 1200 W X-SAR: 1400 W
Fundamental Measurement	radar backscatter (σ^0) interferometric path length
Coverage	60N to 56S
Swath Width	50 km
Incidence Angle	variable, 17°–63°
Mission Length	one 11 day mission in Feb. 2000
Spacecraft	Space Shuttle (STS-99)
Orbit	233 km circular 57° inclination angle
Key Products	topography
Product Resolution	30 m
Product Accuracy	16 m absolute
Data Availability	srtm.usgs.gov

6.5.1.3.6 *Japanese Earth Remote Sensing (JERS-1) SAR* - The Japanese National Space Agency (NASDA) launched JERS-1 (also known as Fuyo-1) into a 570 km (354 mi) orbit on February 11, 1992 (Nemoto et al., 1991; Shimada, 2006). This satellite included a seven band optical sensor and an L-Band SAR which operated at HH polarization. The SAR had a fixed look angle view between 32° and 38° with a swath width of 75 km and a mean resolution of 18 m.

Table 6.33: Sensor characteristics for the JERS-1 SAR.

Sensor	JERS-1 SAR
Sensor Type	SAR
Sensor Scan	fan-beam, SAR
Polarization	HH
Center Frequency	1.275 GHz
PRF	1505-1606 Hz
Operating Bandwidth	15 MHz
Transmit power	1100-1500 W
Fundamental Measurement	radar backscatter (σ°)
Fundamental Resolution	footprint
Coverage	global
Swath Width	75 km
Incidence Angle	32° – 38°
Mission Length	Feb. 1992 – Oct. 1998
Spacecraft	JERS-1
Orbit	570 km sun-synchronous 38.5° inclination angle
Key Products	radar backscatter images
Product Resolution	1 18 m, 100 m
Data Availability	www.asf.alaska.edu eoportal.org

6.5.2 Contemporary Spaceborne Radar Sensors

Currently (early 2008), representatives of each of the major class of active microwave remote sensors are currently flying in earth orbit. The following subsections briefly describe these.

6.5.2.1 Contemporary Altimeters

6.5.2.1.1 *JASON-1 and JASON-2* - A follow-on to Topex/Poseidon, Jason-1 was launched on 7 Dec. 2001. It carries a dual-frequency (C-band and Ku-band) altimeter (Poseidon-2) and a nadir-looking radiometer, the NASA Jason Microwave Radiometer (JMR), which is designed to measure water vapor along the path of the altimeter signal in order to correct the signal path measurement (Jason, 2004). The follow-on Jason-2 is scheduled for launch in June 2008.

Table 6.34: Sensor characteristics for the Jason-1/2 Poseidon-2 Altimeter.

Sensor	(Jason-1/2) Poseidon-2 Altimeter
Sensor Type	altimeter
Sensor Scan	nadir
Polarization	N/A
Center Frequency	C- (5.3 GHz) and Ku-band (13.6 GHz)
Operating Bandwidth	320 MHz
Transmit power	7W
Pulse Length	105 us
PRF	1700 Hz
Fundamental Measurement	time-of-flight (s) radar backscatter (σ^0)
Fundamental Resolution	pulse limited, footprint
Coverage	95% of ice-free oceans in 10 days 66N to 66S
Footprint Shape	circular
Incidence Angle	variable, 0°
Mission Length	Jan. 2002 - present
Spacecraft	Jason-1 & Jason-2
Orbit	1336 km non-sun-synchronous 66° inclination angle
Key Products	10 day repeat cycle sea-level height significant wave height wind speed
Data Availability	podaac.jpl.nasa.gov avisos.cnes.fr

Table 6.35: Sensor characteristics for JMR.

Sensor	Jason-1 Microwave Radiometer (JMR)
Sensor Type	Radiometer
Sensor Scan	nadir
Polarization	N/A
Center Frequency	18.7, 23.8, 34 GHz
Footprint Shape	circular
Incidence Angle	0°
Mission Length	Jan. 2002 - current
Spacecraft	Jason-1
Orbit	1336 km non-sun-synchronous 66° inclination angle 10 day repeat cycle
Fundamental Measurement	Brightness temperature (T_b)
Key Products	atmospheric liquid water water vapor
Data Availability	podaac.jpl.nasa.gov earth.esa.int

6.5.2.2 Contemporary Scatterometers

Currently (early 2008), two scatterometers are operating in Earth orbit, representing the two types of scatterometers: fan-beam and pencil-beam. Primarily designed to measure winds over the ocean, they are also used for land, ice, and vegetation studies.

6.5.2.2.1 QuikSCAT/SeaWinds - Scanning pencil-beam scatterometers such as SeaWinds offer an alternative design to the fan-beam NSCAT and ERS-1/2 scatterometers. This design concept results in smaller, lighter instruments with simpler field-of-view requirements while maintaining a low data rate. As a result, a pencil-beam scatterometer can be more easily accommodated on spacecraft than a fan-beam. A key difference between fan-beam and pencil-beam scatterometers is measurement dwell time. Fan-beam scatterometers permit longer dwell times, albeit with a reduced SNR, compared to a pencil-beam scatterometer system (Spencer et al., 2000, 2003). Though designed as a scatterometer, radiometric measurements useful for rain-flagging can be derived from the data (Jones et al., 2000). The SeaWinds scanning geometry is illustrated in Fig. 6.25.

Two identical copies of the SeaWinds instrument have flown: the first, which was actually the engineering prototype, was launched in 1999 aboard the QuikSCAT mission and is still in operation as of early 2008. The second, flew aboard the ill-fated ADEOS-II (Midori-2) mission for 10 months in 2003.

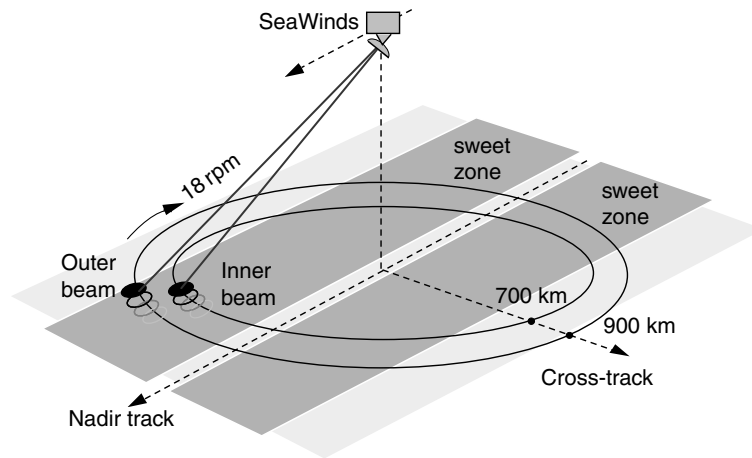


Figure 6.25: Illustration of the SeaWinds measurement geometry showing the 3dB antenna illumination footprints and scanning geometry employed.

Table 6.36: Sensor characteristics for SeaWinds/QuikSCAT.

Sensor	SeaWinds Scatterometer QuikSCAT Scatterometer
Sensor Type	pencil-beam scatterometer
Sensor Scan	dual-scanning pencil-beam
Polarization	outer beam: VV inner beam: HH
Center Frequency	13.6 GHz
Operating Bandwidth	250 kHz
Transmit power	110 W
Pulse Length	1.5 ms
PRF	192 Hz (two beams)
Fundamental Measurement	radar backscatter (σ^0)
Fundamental Resolution	footprint
Radiometric Accuracy (K_p)	0.02-0.07
Radiometric Stability ($\pm\sigma^0$)	0.1 dB
Coverage	global, 2 days
Swath Width	1800 km
Footprint Shape	elliptical
Footprint Size	20×30 km , 25×35 km
Incidence Angle	variable, 17°–60°
Mission Length	QuikSCAT: 1999 to present SeaWinds/ADEOS-II: 2003
Spacecraft	QuikSCAT, ADEOS-II (Midori-II)
Orbit	795 km sun-synchronous
Key Products	ocean winds radar backscatter
Product Resolution	25 km
Product Accuracy	2 m/s, 20°
Product Range	0-50 m/s
Data Availability	winds and backscatter : podaac.jpl.nasa.gov winds : www.remss.com backscatter images : www.scp.byu.edu winds : www.remss.com

6.6.2.2 *Advanced Scatterometer (ASCAT)* - The advanced scatterometer (ASCAT) is a follow-on for the ERS-1/2 scatterometer series (Figa-Saldaña et al., 2002). The first ASCAT was launched in 2006 aboard the meteorological (MetOp-A) platform. Two additional launches are planned in later years. Generally similar to the European Remote Sensing (ERS) ERS-1 and ERS-2 Advanced Microwave Instrument (AMI) in scatterometer mode, ASCAT uses multiple fan-beam antennas to make σ^o measurements at different azimuth angles over a wide swath. However, ASCAT has a dual-sided swath to provide additional coverage (see Fig. 6.26) and the resolution is improved to 25 km on a 12.5 km grid. The range of incidence angles relative to ESCAT is increased to improve wind measurement accuracy, though this increases the sensitivity to rain.

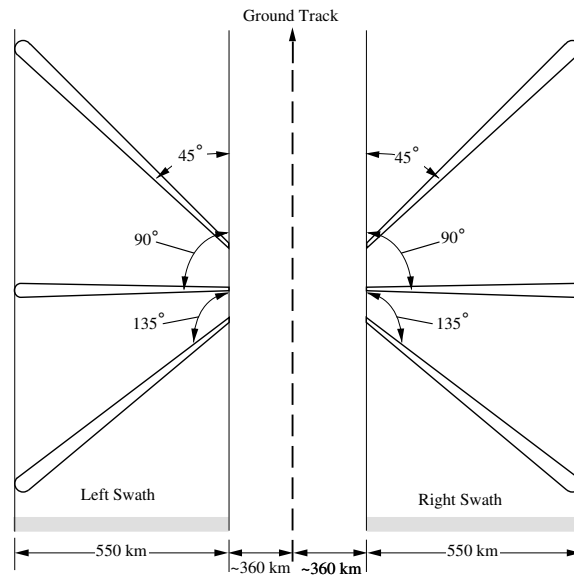


Figure 6.26: Illustration of the ASCAT measurement swath geometry. Range gate filtering resolves the footprints into smaller areas.

Table 6.37: Sensor characteristics for ASCAT.

Sensor	ASCAT
Sensor Type	range-gate, scatterometer
Sensor Scan	fan-beam, 6-beams, dual sided
Polarization	VV
Center Frequency	5.255 GHz
Pulse Length	8.03 ms & 10.1 ms
PRF	29.12 Hz
Operating Bandwidth	401 kHz & 242 kHz
Transmit power	125 W
Fundamental Measurement	radar backscatter (σ^0)
Fundamental Resolution	footprint
Radiometric Accuracy (K_p)	3.3% to 9.9%
Radiometric Stability ($\pm\sigma^0$)	0.46 dB
Coverage	global
Swath Width	dual 550 km swaths
Footprint Shape	fan-beam, averaged
Incidence Angle	variable, 25°–65°
Mission Length	5 years
Spacecraft	MetOp
Orbit	822 km sun-synchronous, 21:30 ascending node 98.7° inclination angle 29 day and 5 day repeat cycles
Key Products	ocean winds radar backscatter ice products soil moisture
Product Resolution	50 km & 25 km posted on 25 km and 12.5 km grids
Product Accuracy	2 m/s, 20°
Product Range	0-35 m/s
Data Availability	www.meteorologie.eu.org/safo

6.5.2.3 Contemporary SARs

As of early 2008, several earth-observing SARs are operating in Earth orbit, providing high resolution radar imagery at L-, C-, and X-band. Selected sensors are considered below.

6.5.2.3.1 ERS-1/2 AMI SAR - The ERS-1 and ERS-2 Advanced Microwave Instrument (AMI) in SAR mode collects C-band SAR image data in a number of modes (Attema, 1991). In addition to conventional high resolution SAR images, the AMI SAR can be operated in “wave mode” in which lower resolution images are collected over a wide swath in order to estimate ocean wave spectra. Power and thermal considerations limit the time the instrument can be operated each orbit to about 12 minutes per orbit.

Table 6.38: Sensor characteristics for ERS-1/2 AMI SAR Mode.

Sensor	ERS-1/2 AMI SAR Mode
Sensor Type	SAR, wave mode SAR
Sensor Scan	SAR, wide-beam SAR
Polarization	VV
Center Frequency	5.3 GHz
Operating Bandwidth	15.55 MHz
Transmit power	5 kW
Pulse Length	37 μ s
PRF	1640-1720 Hz
Fundamental Measurement	radar backscatter (σ^0)
Fundamental Resolution	16 m
Radiometric Accuracy (K_p)	<2.5 dB at $\pm\sigma^0 = -18$ dB
Radiometric Stability ($\pm\sigma^0$)	0.95 dB
Coverage	limited
Swath Width	20 km, (image mode) 80 km, (wave mode) 500 km
Footprint Shape	push-broom
Incidence Angle	variable, 18°–20°, 18°–50°
Mission Length	ERS-1: 1992-96 ERS-2: 1996-
Spacecraft	ERS-1, ERS-2
Orbit	785 km sun-synchronous (100 min period) 98.5° inclination angle 35 day repeat cycle (3 and 168 also used)
Key Products	radar backscatter ocean wave spectra sea ice
Product Resolution	16 m, 30m, 100 m
Data Availability	www.esa.int www.asf.alaska.edu

6.5.2.3.2 *RADARSAT* - The RADARSAT-1 satellite was launched on 4 Nov. 1995. It's primary sensor is a SAR system capable of multiple operational modes. The main beam is steerable. RADARSAT is operated as a commercial venture by the Canadian government. Unlike many other sensors, data must be purchased. Cost of data is often a limiting factor in studies using this sensor. The RADARSAT SAR has seven beam modes with different resolutions and coverage².

Table 6.39: RADARSAT-1 SAR modes.

Mode	Resolution	Incidence angles	Swath width
Standard	25 m	20-49°	100 km
Wide	25 m	20-45°	150 km
Extended Low	25 m	10-20°	75 km
Extended High	25 m	50-60°	75 km
Fine	9 m	35-49°	50 km
ScanSAR Wide	100 m	20-50°	500 km, 440 km
ScanSAR Narrow	50 m	20-46°, 32-46°	300 km

²http://www.ccrs.nrcan.gc.ca/ccrs/data/satsens/radarsat/specs/radspec_e.html

Table 6.40: Sensor characteristics for RADARSAT-1 SAR.

Sensor	RADARSAT-1 SAR
Sensor Type	SAR, wave mode SAR
Sensor Scan	SAR, scanSAR
Polarization	VV
Center Frequency	5.3 GHz
Fundamental Measurement	radar backscatter (σ^0)
Fundamental Resolution	16 m
Radiometric Stability ($\pm\sigma^0$)	0.3 dB
Coverage	global, 4-5 days
Swath Width	50–500 km
Footprint Shape	push-broom
Incidence Angle	variable, 10°–59°
Mission Length	Nov. 1995 to present
Spacecraft	RADARSAT-1
Orbit	798 km, sun-synchronous, 18:00 ascending node 98.6° inclination, 100.7 min period
Key Products	radar backscatter images sea ice
Product Resolution	8–100 m
Data Availability	www.rsi.ca www.asf.alaska.edu

6.5.2.3.3 ALOS PALSAR - The Phased Array type L-band Synthetic Aperture Radar (PALSAR) is an improved version of the JERS-1 SAR and was developed as a joint project between the Japanese space agency (JAXA) and the Japan Resources Observation System Organization (JAROS) (Rozenqvist et al., 2007; Wakabayashi et al., 1998). PALSAR is part of the Advanced Land Observing Satellite (ALOS), also known as Daichi, launched on 24 Jan. 2006. PALSAR is capable of wideswath (scanSAR), as well as polarimetric operation. ALOS also carries the Advanced Visible and Near Infrared Radiometer type 2 (AVNIR-2) and the Panchromatic Remote-Sensing Instrument for Stereo Mapping (PRISM).

Table 6.41: Sensor characteristics for PALSAR.

Sensor	ALOS PALSAR
Sensor Type	SAR
Sensor Scan	fan-beam, SAR
Polarization	HH, HV, VH, VV
Center Frequency	1.270 GHz
PRF	1505-1606 Hz
Operating Bandwidth	14 or 28 MHz
Transmit power	2000 W
Fundamental Measurement	radar backscatter (σ^0)
Fundamental Resolution	footprint
Radiometric Accuracy (K_p)	1 dB
Radiometric Stability ($\pm\sigma^0$)	1.5 dB
Coverage	global
Swath Width	Fine: 30-70 km ScanSAR: 240-350 km
Incidence Angle	9.9°–50.8°
Mission Length	Jan. 2006 to present
Spacecraft	ALOS
Orbit	692 km sun-synchronous 98.16° inclination angle 46 day repeat cycle
Key Products	radar backscatter images
Product Resolution	10-157 m, depending on mode
Data Availability	www.eorc.jaxa.jp www.palsar.ersdac.or.jp envisat.esa.int www.asf.alaska.edu www.alos-restec.jp

6.5.2.3.4 *EnviSAT Advanced SAR (ASAR)* - The European Space Agency (ESA) launched the Envisat in March 2002. It includes an Advanced SAR (ASAR) sensor. Operating at C-band, ASAR continues the SAR image dataset started with ERS-1/2 but includes dual polarization capability. EnviSAT also carries the RA-2 radiometer. Envisat is operated as a commercial venture and data must be purchased (see http://earth.esrin.esa.it/pub/ESA_DOC/ENVISAT/ENVI87.pdf).

The Envisat ASAR operates in imaging mode similar to the ERS-1/2 AMI SAR with wide swath mode (400 km swath, 150 m resolution, single polarization) and an alternating polarization (56-100 km swath, 25 m resolution, selectable HH polarization) mode. It employs seven selectable beams with an active phased array antenna.

Table 6.42: Sensor characteristics for Envisat ASAR.

Sensor	Envisat ASAR
Sensor Type	SAR, wave mode SAR
Sensor Scan	SAR, wide-beam SAR
Polarization	VV, HH, VH, HV
Center Frequency	5.331 GHz
Operating Bandwidth	50 MHz
Transmit power	5 kW
Fundamental Measurement	radar backscatter (σ^0)
Fundamental Resolution	16 m
Radiometric Accuracy (NSE)	~ -25 dB
	worst-case better than -20 dB
Radiometric Resolution	1.5-3.5 dB
Radiometric Stability ($\pm\sigma^0$)	0.3 dB
Coverage	global
Swath Width	20 km, 100 km, 400 km
Footprint Shape	push-broom
Footprint Size	30 m \times 30 m, 150 m \times 150 m, 1 km \times 1 km
Incidence Angle	variable, $15^\circ - -45^\circ$
	$14.5^\circ - 22.1^\circ$ 104 km swath
	$18.8^\circ - 26.1^\circ$ 103 km swath
	$25.8^\circ - 31.2^\circ$ 82 km swath
	$30.8^\circ - 36.1^\circ$ 89 km swath
	$35.7^\circ - 39.3^\circ$ 64 km swath
	$39.0^\circ - 42.7^\circ$ 71 km swath
	$42.5^\circ - 45.2^\circ$ 57 km swath
Mission Length	Dec. 2007 to present
Spacecraft	Envisat
Orbit	800 km sun-synchronous (101 min period)
	98° inclination angle
	35 day repeat cycle
Key Products	radar backscatter
	ocean wave spectra
Product Resolution	30 m, 150 m, 1 km
Data Availability	envisat.esa.int

6.5.2.3.5 *TerraSAR-X* - TerraSAR-X is a German X-band SAR similar to X-SAR, but with additional capability including spotlight, stripmap, and scansar modes (Stangl et al., 2006). It also supports interferometric operation via a second spacecraft (Krieger et al., 2007). The highly capable TerraSAR-X was launched on 15 June 2007.

Table 6.43: Sensor characteristics for TerraSAR-X.

Sensor	TerraSAR-X
Sensor Type	SAR, interferometric SAR
Sensor Scan	SAR, wide-beam SAR
Center Frequency	9.65 GHz
Operating Bandwidth	5-300 MHz, 150 MHz nominal
Transmit power	2260 W
PRF	3-6.5 kHz
Fundamental Measurement	radar backscatter (σ^0)
Fundamental Resolution	spotlight: 1-2 m stripmap: 3-6 m scanSAR: 16 m
Radiometric Accuracy (NSE)	~ -25 dB worst-case better than -20 dB
Radiometric Resolution	1.5-3.5 dB
Radiometric Stability ($\pm\sigma^0$)	0.3 dB
Coverage	global
Swath Width	spotlight 10 km stripmap: 30 km scanSAR: 100 km
Footprint Shape	push-broom
Incidence Angle	variable, $15^\circ - -60^\circ$
Mission Length	June 2007 to present
Spacecraft	TerraSAR-X
Orbit	514.8 km sun-synchronous 18:00 ascending node 97.44° inclination angle 11 day repeat cycle
Key Products	radar backscatter DEM
Data Availability	www.dlr.de

6.5.2.3.6 *Okean* - The Russian Okean satellite series included a number of microwave radar remote sensors. For example, the Okean-O satellite had a side-looking real aperture radar (RLSBO-D) with a swath width of 700 km and a resolution of 1.5 km × 2 km and a Delta-2 scanning radiometer with a swath width of 900 km and a resolution of 16 km × 21 km [<http://www.astronautix.com/craft/okeano.htm>]. It is not clear what data is available from these sensors.

6.5.2.3.7 *Almaz* - Since the Russian Almaz are a series of real-aperture radar imagers, they are not technically SARs, but are included in this section since they are designed for radar imaging. The first Almaz was flown in 1987. Another Almaz³ was launched in 1991. The SAR used two 0.5 x 15 m slotted waveguide antennas.

Table 6.44: Sensor characteristics for Almaz.

Sensor	Almaz
Sensor Type	real-aperture imager
Sensor Scan	fan-beam, range-compressed
Center Frequency	3 GHz
Transmit power	190 kW (peak)
Fundamental Measurement	radar backscatter (σ^0)
Fundamental Resolution	15-30 m
Coverage	limited
Swath Width	20-45 km
Incidence Angle	variable
Mission Length	18 months
Spacecraft	Almaz-1
Key Products	radar backscatter images
Product Resolution	15-30 m

6.5.2.4 Contemporary Weather Radars

Ground-based weather radars have been extensively deployed to study rainfall. However, only spaceborne weather radars are considered here. One of the most important rain radars that has flown to date is the TRMM precipitation radar. Cloudsat carried a related radar designed to measure clouds.

³<http://www.globalsecurity.org/space/world/russia/almaz.htm>

6.5.2.4.1 *Tropical Rain Measuring Mission (TRMM) Precipitation Radar (PR)* - The TRMM PR was orbited in 1995 (Awaka et al., 1997; Meneghini et al., 2000). It uses electronic switching of 128 antenna elements in a 2 m by 2 m antenna to provide 49 fixed beams in a cross-track push-broom configuration over a 220 km wide swath (see Fig. 6.27). The PR employs pulse compression to provide 250 m vertical resolution measurements of atmospheric scattering and attenuation from which rain rate estimates are derived. Surface backscatter data is also used in ocean wind speed, land cover, and vegetation studies. TRMM has far exceeded its design life and has provided an extensive data set over the tropics (latitude less than $\pm 30^\circ$). TRMM PR data is augmented by TMI radiometer data.

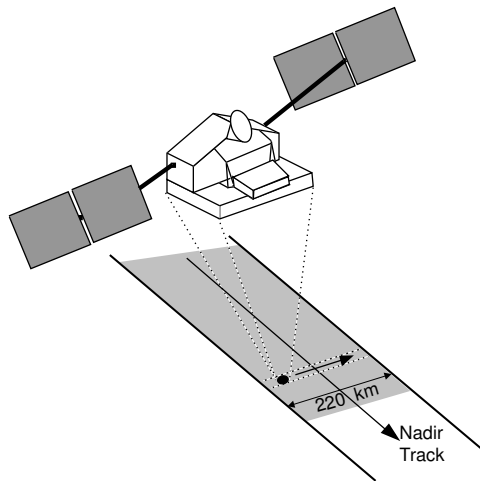


Figure 6.27: An illustration of the TRMMPR measurement geometry. Switched antenna elements form 48 different spot beams across the swath that are used in sequence to scan across the swath. Each beam operates at a different incidence angle.

Table 6.45: Sensor characteristics for TRMM PR.

Sensor	TRMM PR
Sensor Type	Precipitation radar
Sensor Scan	electronically switched pencil-beam in push broom configuration
Polarization	H
Center Frequency	13.8 GHz
Operating Bandwidth	6 MHz
Transmit power	500 W
Pulse Length	1.67 μ s
PRF	2776 Hz
Vertical Resolution	250 m
Coverage	40S to 40N
Swath Width	220 km
Footprint Shape	elliptical
Footprint Size	4.3 \times 4.3 km to 5.0 \times 5.8 km
Beamwidth	$\sim 71^\circ$
Incidence Angle	$\pm 17^\circ$
Mission Length	Dec. 1995 to present
Spacecraft	TRMM
Orbit	350 km high circular, semi-equatorial 402.5 km high after Aug. 2001
Fundamental Measurement	Brightness temperature (T_b)
Key Products	vertical and horizontal distribution of precipitation
Product Resolution	4.3 km (nadir) 5 km (swath edge)
Product Accuracy	min Z: 20.8 dBZ
Product Range	0-15 km
Data Availability	www-dsdis.gsfc.nasa.gov

6.5.2.4.2 *CloudSat Cloud Profiling Radar (CPR)* - The CPR was orbited as part of the CloudSat mission in 2007. The CPR is a nadir-looking 94 GHz radar that is designed to measure the backscatter as a function of range (height) in clouds (Stephens et al., 2002). Its spatial coverage is limited to very close to the nadir track,

Table 6.46: Sensor characteristics for CPR.

Sensor	CloudSat CPR
Sensor Type	cloud profiling radar
Sensor Scan	nadir-looking pencil-beam
Polarization	circular
Center Frequency	94 GHz
Operating Bandwidth	6 MHz
Pulse Length	3.3 μ s
PRF	4300 Hz
Radiometric Accuracy (min detectable Z)	-25 dBZ
Radiometric Stability ($\pm\sigma^o$)	1.5 dB
Vertical Resolution	500 m
Vertical Range	0-25 km
Swath Width	1.4 km
Footprint Shape	circular
Footprint Resolution	1.4 km \times 2.5 km
Mission Length	April 2006 to present
Spacecraft	Cloudsat
Orbit	705 km altitude, circular
Fundamental Measurement	reflectivity versus range
Key Products	vertical distribution of water droplets
Product Accuracy	min Z -30.8 dBZ
Product Range	0-15 km
Data Availability	www.cira.colostate.edu

6.5.3 Future Radar Sensors

Many new spaceborne active microwave sensors are in various planning stages in the U.S., Japan, Europe, China, and India. Many of these are extensions of existing missions. Many new missions are also planned. It is not possible to do anything more than describe a few of them.

6.5.3.1 RADARSAT2

RADARSAT-2 is a follow-on to RADARSAT-1 but with additional capabilities, including high resolution, multipolarization and both left- and right-looking imaging. Like RADARSAT-1, RADARSAT-2 will be operated as a commercial venture by the Canadian government. Unlike many other sensors, data must be purchased. RADARSAT-2 was successfully launched on 14 Dec. 2007. Like RADARSAT-1, RADARSAT-2 SAR has eleven operational beam modes⁴.

Table 6.47: RADARSAT-2 SAR modes and resolutions.

RADARSAT-2 Mode	Resolution	Incidence angles	Swath width
Standard	25 m	20-49°	100 km
Wide	25 m	20-45°	150 km
Low Incidence	35 m	20-23°	170 km
High Incidence	24 m	50-60°	70 km
Fine	10 m	37-49°	50 km
ScanSAR Wide	100 m	20-49°	500 km
ScanSAR Narrow	50 m	20-46°	300 km
Standard Quad Polarization	27 m	20-41°	25 km
Fine Quad Polarization	10 m	20-41°	25 km
Multi-Look Fine	10 m	30-50°	50 km
Ultra-fine	3 m	30-40°	20 km

⁴http://www.ccrs.nrcan.gc.ca/ccrs/data/satsens/radarsat/rsat2/mission_e.html

Table 6.48: Sensor characteristics for the RADARSAT-2 SAR.

Sensor	RADARSAT-2 SAR
Sensor Type	SAR, wave mode SAR
Sensor Scan	SAR, scanSAR
Polarization	HH, HV, VH, VV
Center Frequency	5.405 GHz
Operating Bandwidth	100 MHz
PRF	variable
Fundamental Measurement	radar backscatter (σ^0)
Fundamental Resolution	mode dependent
Radiometric Stability ($\pm\sigma^0$)	0.3 dB
Coverage	global, equator: 2-3 days north of 70N: daily
Swath Width	50–500 km
Footprint Shape	push-broom
Incidence Angle	variable, 10°–59°
Mission Length	7 years
Spacecraft	RADARSAT-2
Orbit	798 km, sun-synchronous, 214 day repeat 98.6° inclination angle 100.7 min period
Key Products	radar backscatter images sea ice
Product Resolution	3–100 m

6.5.3.2 *Aquarius* - The planned *Aquarius* mission includes both a radiometer and a scatterometer and is designed to make precise global observations of sea surface salinity from space. The *Aquarius* sensor suite is described in Section 6.3.3.

6.5.4 Extra-Terrestrial Radar Sensors

A variety of earth-based microwave sensors have been used in astronomical observations. Both active and passive sensing have been used. Passive radio telescopes are extensively employed for the study of extra-solar objects (Burke and Graham-Smith, 2002; Rohlfs and Wilson, 1996; Verschuur et al., 1987); however, ground-based radars have been used to study the moon and other planets (Evans and Hagfors, 1968; Pettengill, 1970; Plaut and Arvidson, 1992). Spacecraft-based imaging radar systems have been deployed to study cloud-covered Venus, and more recently, Titan. Here, brief descriptions of several of these sensors are provided.

The dense cloud cover of Venus precludes conventional optical sensing of the surface, necessitating the use of radar to probe beneath the thick atmosphere. A number of U.S. and Russian spacecraft have carried radar systems designed to image through the atmosphere. Both the U.S. Magellan mission (Pettengill et al., 1991) and the Russian Venera 15 and 16 probes (Bogomolov et al., 1985) carried radar sensors which combined SAR and altimeter functions.

6.5.4.1 Pioneer Venus Orbiter Radar

The Pioneer Venus Orbiter Radar is described in (Cuttin et al., 1984; Dallas, 1987).

6.5.4.2 Venera SAR

In 1983 the two Soviet Venera 15 and 16 spacecraft began their missions to orbit Venus. Operating in tandem, the two identical spacecraft carried SAR systems designed to image the surface (Bogomolov et al., 1985; Ivanov, 1990). The SAR antenna was 6 m by 1.4 m while the altimeter antenna was 1 m in diameter. A separate 2.6 m antenna was used for communication to the earth.

Table 6.49: Sensor characteristics for Venera SAR.

Sensor	Venera 15/16 Radars
Sensor Type	SAR
Sensor Scan	fan-beam SAR
Center Frequency	3.75 GHz
Pulse Length	1.54 μ s
PRF	burst, 127 pulses/burst
Transmit power	8 W
Fundamental Measurement	radar backscatter
Fundamental Resolution	SAR
Coverage	25% of Venus surface south of 30N
Swath Width	130 km
Mission Length	8 months beginning in 1984
Spacecraft	Venera 15 & 16
Orbit	elliptical, apsis of 1000 km
Key Products	radar backscatter image
Product Resolution	1-2 km
Data Availability	nssdc.gsfc.nasa.gov

6.5.4.3 Magellan

The Magellan mission was launched on 4 May 1989. It went into an orbit around Venus on 10 Aug. 1990 and carried a radiometer, an altimeter (ALTA), and a synthetic aperture radar (Dallas and Nickle, 1987; Pettengill et al., 1991; Rokey, 1993; Saunders et al., 1992, 1990). To save cost and weight, the main 3 m antenna was shared between the SAR sensor and communications. A 189 minute elliptical orbit was designed to bring the spacecraft close to the surface to improve the imaging signal-to-noise ratio at the orbit perigee. Data collected during the perigee was recorded during collection and broadcast to earth during the apogee. To account for the variable altitude, a complicated burst-mode transmit timing was used for SAR imaging with radiometer and altimeter measurements were interleaved with the SAR measurements. The received data was compressed for transmission to Earth. At the end of the mission the spacecraft was slowed and allowed to enter the atmosphere.

Table 6.50: Sensor characteristics for the Magellan SAR.

Sensor	Magellan SAR
Sensor Type	SAR
Sensor Scan	fan-beam SAR
Polarization	HH
Center Frequency	2.385 GHz
Pulse Length	26.5 μ s
PRF	burst, 4.4-5.8 kHz
Operating Bandwidth	2.26 MHz
Transmit power	325 W
Fundamental Measurement	radar backscatter
Fundamental Resolution	SAR
Radiometric Accuracy (K_p)	
Radiometric Stability ($\pm\sigma^o$)	
Coverage	90% of Venus surface south of 30N
Swath Width	25 km
Footprint Shape	circular
Footprint Size	25 km
Incidence Angle	variable
Mission Length	10 Aug. 1990 – 11 Oct. 1994
Spacecraft	Magellan
Orbit	elliptical, 189 min period
Key Products	radar backscatter image
Product Resolution	150 m SAR, 30 m altimeter
Data Availability	www.lpi.usra.edu/library/RPIF pds.jpl.nasa.gov

6.5.4.4 *Cassini* - The Cassini radar instrument shares the main radio dish used for communication between the Cassini spacecraft and Earth and is capable of radiometer, altimeter, scatterometer and SAR measurements, all operating at the same frequency of 13.78 GHz. The instrument was designed to image through Titan's cloud cover using 5 antenna beams from its main 4 m high-gain antenna. Spatial resolution of the radiometer and altimeter is dependent on the range from the Cassini spacecraft and the surface, which is highly variable.

Table 6.51: Sensor characteristics for the Cassini Radar.

Sensor	Cassini Radar
Sensor Type	altimeter/scatterometer/SAR
Sensor Scan	pencil-beam scanned by spacecraft motion
Center Frequency	13.78 GHz
PRF	variable burst
Operating Bandwidth	scatterometer: 117 kHz altimeter: 4.68 MHz
Fundamental Measurement	radar backscatter, range
Fundamental Resolution	variable
Coverage	20% of Titan
Footprint Shape	elliptical
Mission Length	2004 to present
Spacecraft	Cassini
Key Products	radar backscatter, height
Product Resolution	variable SAR: 300 m to 2 km altimeter: 24-27 km horizontal 90-140 m vertical
Data Availability	pds.jpl.nasa.gov

Bibliography

- I.S. Ashcraft and D.G. Long, "Observation and Characterization of Radar Backscatter over Greenland," *IEEE Transactions on Geoscience and Remote Sensing*, Vol. 43, No.2, pp. 237-246, 2004.
- J. Awaka, T. Iguchi, H. Kumagai and K. Okamoto, "Rain type classification algorithm for TRMM precipitation radar," *Proceedings of the IEEE 1997 International Geoscience and Remote Sensing Symposium*, August 3-8, Singapore, pp. 1636-1638, 1997.
- E. Attema, "The Active Microwave Instrument Onboard the ERS-1 Satellite," *Proceedings of the IEEE*, Vol. 79, No. 6, pp. 791-799, 1991.
- E.P.W. Attema, G. Duchossois, G. Kohlhammer, "ERS-1/2 SAR land applications: overview and main results", *Proc. IEEE Int. Geoscience and Remote Sensing Symposium*, pp 1796-1798, 1998.
- J. Bamber, "A digital elevation model of the Antarctic ice sheet derived from ERS-1 altimeter data and comparison with terrestrial measurements," *Annals of Glaciology*, Vol. 20, pp. 48-54, 1994.
- D.E. Barrick and C.T. Swift, "The Seasat Microwave Instruments in Historical Perspective," *IEEE J. Oceanic Eng.*, Vol. OE-5, No. 2, pp 74-79, 1980.
- C. Bennett, A.J. Banday, K.M. Gorski, G. Hinshaw, et al., "Four-Year COBE DMR Cosmic Microwave Background Observations: Maps and Basic Results," *The Astronomical Journal*, Vol. 464, pp. L1-L4, June 1996.
- W. Berg and C. Kummerow, "The Climate Rainfall Data Center," *Bulletin of the American Meteorological Society*, pp. 1237-1240, Sep. 2005.
- R. Bernard, A. Le Cornec, L. Eymard, and L. Tabary, "The Microwave Radiometer Aboard ERS-1, Part 1: Characteristics and Performances," *IEEE Transactions on Geoscience and Remote Sensing*, Vol. 31, No. 5, pp. 1186-1198, Sept. 1993.

- S.M. Bhandari, M.K. Dash, N.K. Vyas, A. Khanolkar, N. Sharma, N. Khare, and P.C. Pandey, "Intercomparison of simultaneous MSMR and SSM/I observations for sea ice estimation over Antarctic region," *ISPRS Tech. Comm. VII International Symposium on Resources and Environmental Monitoring*, pp. 409-413, Hyderabad, India, Dec. 3-6, 2002.
- I.J. Birrer, E.M. Bracalente, G.J. Dome, J. Sweet, and G. Berthold, " σ^0 Signature of the Amazon Rainforest Obtained from the Sesat Scatterometer," *IEEE Transactions on Geoscience and Remote Sensing*, Vol. Ge-20, No. 1, pp. 11-17, 1982.
- A.F. Bogomolov, N.V. Zherikhin, and G.A. Sokolov, "Venera 15 and 16: Synthesized Aperture Radar in Orbit Around Venus," *Radio, Physics and Quantum Electronics*, Vol. 28, No. 3, pp. 169-181, March 1985.
- G.H. Born, J.A. Dunne, and D.B. Lamb, "Seasat mission overview," *Science*, Vol. 204, pp. 1405-1406, 1979.
- B.F. Burke and F. Graham-Smith, *An Introduction to Radio Astronomy*, Cambridge, UK; New York: Cambridge University Press, 2002.
- D.J. Cavalieri, P. Gloersen, and W. J. Campbell, "Determination of sea ice parameters with the NIMBUS-7 SMMR," *J. Geophys. Res.*, Vol. 89, No. D4, pp. 5355-5369, 1984.
- I.V. Cherny and V.Y. Raizer, *Passive Microwave Remote Sensing of Oceans*, New York, NY: John Wiley, 1998.
- J. Cimino, C. Elachi, M. Settle, "SIR-B-The Second Shuttle Imaging Radar Experiment," *IEEE Transactions on Geoscience and Remote Sensing*, Vol. GE-24, No. 4, pp. 445-452, July 1986.
- M. Coltelli, G. Fornaro, G. Franceschetti, R. Lanari, M. Migliaccio, J. R. Moreira, K. P. Papathanassiou, G. Puglisi, D. Riccio, and M. Schwabisch, "SIR-C/X-SAR multifrequency multipass interferometry: A new tool for geological interpretation," *Journal Of Geophysical Research*, Vol. 101, pp. 23127-23148, 1996.
- M. Colton and G. Poe, "Intersensor Calibration of DMSP SSM/I's: F-8 to F-14; 1987-97," *IEEE Transactions on Geoscience and Remote Sensing*, Vol. 37, Jan. 1999.
- E. Cutting, J.H. Kwok, and S.N. Mohan, "The Venus radar mapper mission," *J. Brit. Interplan. Soc.*, Vol. 37, pp. 443-452, 1984.

- J.C. Curlander and R.N. McDonough, *Synthetic Aperture Radar: Systems and Signal Processing*, John Wiley and Sons, Inc., New York, NY, 1991.
- S.S. Dallas, "The Venus radar mapper mission," *Acta Astronautica*, Vol. 15, No. 2, pp. 105-124, 1987.
- S.S. Dallas and N.L. Nickle, "The Magellan mission to Venus. Advances in astronomical sciences. Part 1," *Aerospace Century 21*, AAS 86-331, 64, 1987.
- R.J. Doviak, D.S. Zrnic, and D.S. Sirmans, "Doppler Weather Radar", *Proc. IEEE*, Vol. 67, pp. 1522-1553, Nov. 1979
- R.J. Doviak, and D.S. Zrnic, *Doppler Radar and Weather Observations*, Orlando: FL: Academic Press, Inc.; 1984.
- D.S. Early and D.G. Long, "Azimuth Modulation of C-band Scatterometer sigma-0 Over Southern Ocean Sea Ice," *IEEE Transactions on Geoscience and Remote Sensing*, Vol. 35, No. 5, pp. 1201-1209, 1997.
- D.S. Early and D.G. Long, "Image Reconstruction and Enhanced Resolution Imaging From Irregular Samples," *IEEE Transactions on Geoscience and Remote Sensing*, Vol. 39, No. 2, pp. 291-302, 2001.
- C. Elachi and J.J. van Zyl, *Introduction to the Physics and Techniques of Remote Sensing*, John Wiley & Sons, Inc., Hoboken: New Jersey, 2006.
- C. Elachi, *Spaceborne Radar Remote Sensing: Applications and Techniques*, IEEE, New York, NY, 1988.
- C. Elachi and F.T. Ulaby, *Radar Polarimetry for Geoscience Applications*, Artech House, 2000.
- C. Elachi, L.E. Schaber, and G.G. Schaber, "Spaceborne radar subsurface imaging in hyperarid regions," *IEEE Trans. Geosci. and Rem. Sens.*, GE-22, No. 4, 383-388, 1984.
- J.V. Evans and T. Hagfors (eds), *Radar Astronomy*, New York, NY: McGraw-Hill, 1968.
- D.L. Evans, J.J. Plaut, E.R. Stofan, "Overview of the Spaceborne Imaging Radar-C/X-Band Synthetic-Aperture Radar (SIR-C/X-SAR) Missions," *Remote Sensing of Environment*, Vol. 59, No. 2, pp. 135-140, 1997.
- T.G. Farr, et al., "The Shuttle Radar Topography Mission," *Rev. Geophys.*, Vol. 45, RG2004, doi:10.1029/2005RG000183, 2007.

- R. Ferraro, F. Weng, N. Grody, and A. Basist, "An Eight Year (1987-1994) Time Series of Rainfall, Clouds, Water Vapor, Snow-cover, and Sea-ice Derived from SSM/I Measurements," *Bulletin of the American Meteorological Society*, pp. 891-905, May 1996.
- A. Freeman, "SAR Calibration: An Overview," *IEEE Trans. Geosci. Remote Sensing*, Vol. 30, No. 6, pp. 1107-1121, 1992.
- J. Figa-Saldaña, J.J.W. Wilson, E. Attema, R. Gelsthorpe, M.R. Drinkwater, and A. Stofflen, "The Advanced Scatterometer (ASCAT) on the Meteorological Operational (MetOp) Platform: A Follow on for European Wind Scatterometers," *Can. J. Remote Sensing*, Vol. 28, No. 3, pp. 404-412, 2002.
- R.E. Fischer, "Standard Deviation of Scatterometer Measurements from Space," *IEEE Trans. on Geoscience Electronics*, Vol. GE-10, No. 2, pp. 106-113, 1972.
- J. Font, Y. Kerr, and M. Berger, "Measuring Ocean Salinity from Space: the European Space Agency's SMOS Mission," *Backscatter*, Vol. 11, pp. 17-19, 2000.
- R.R. Forster, D.G. Long, K.C. Jezek, S.D. Drobot, and M.R. Anderson, "The Onset of Arctic Sea-Ice Snowmelt as Detected with Passive- and Active-microwave Remote Sensing," *Annals of Glaciology*, Vol. 33, pp. 85-93, 2001.
- L-L Fu and B. Holt, "Seasat Views Ocean and Sea Ice with Synthetic Aperture Radar," Jet Propulsion Laboratory Publication 81-120, Pasadena, CA, 1982.
- L-L Fu, E.J. Christensen, C.A. Yamarone Jr., M. Lefebvre, Y. Menard, M. Dorrer, and P. Escudier, "TOPEX/POSEIDON mission overview," *Journal of Geophysical Research*, Vol. 99, No. C12, pp. 24369-24381, 1994.
- L-L fu, A. Cazenave, *Satellite Altimetry and Earth Sciences: a Handbook of Techniques and Application*, Orlando: FL: Academic Press, Inc.; 2001.
- A.K. Fung, *Microwave Scattering and Emission Models and Their Applications*, Norwood, MA: Artech House, Inc., 1994.
- P.W. Gaiser, et al., "The WindSat Space Born Polarimetric Microwave Radiometer: Sensor description and early Orbit Performance," *IEEE Trans. Geosci. Rem. Sens.*, Vol. 42, No. 11, 2347-2361, 2004.
- P. Gloersen and F.T. Barath, "A Scanning Multichannel Microwave Radiometer for Nimbus-G and SeaSat-A," *IEEE Journal of Oceanic Engineering*, Vol.2, pp. 172-178, 1977.

- P. Gloersen, D.J. Cavalieri, A.T.C. Chang, T.T. Wilheit, W.J. Campbell, O.M. Johannessen, K.B. Katsaros, K.F. Kunzi, D.B. Ross, D. Staelin, E.P.L. Windsor, F.T. Barth, P. Gudmandsen, E. Langham and R.O. Ramseier, "A summary of results from the first NIMBUS-7 SMMR observations," *Journal of Geophysical Research*, Vol. 89, pp. 5335-5344, 1987
- M.A. Goodberlet, "Improved Image Reconstruction Techniques for Synthetic Aperture Radiometers," *IEEE Trans. Geosci. Remote Sensing*, Vol. 38, no. 3, pp. 1362-1366, May 2000.
- W.L. Grantham, *et al.*, "The Seasat-A satellite scatterometer," *IEEE J. Oceanic Eng.*, vol. OE-2, pp. 200-206, 1977.
- W.L. Grantham, E.M. Bracalente, C.L. Britt, Jr., F.J. Wentz, W.L. Jones, Jr., and L. C. Schroeder, "Performance Evaluation of an Operational Spaceborne Scatterometer," *IEEE Trans. Geosci. Remote Sens.*, Vol. GE-20, No. 3, July 1982.
- N.C. Grody, "Classification of Snow Cover and Precipitation Using the Special Sensor Microwave/Imager," *Journal of Geophysical Research*, Vol. 94, pp. 7423-7435, April 1991.
- R. Hanssen, *Radar Interferometry: Data Interpretation and Error Analysis*, Kluwer Academic, London, 2001.
- F.M. Henderson and A.J. Lewis, ed., *Principles and Applications of Imaging Radar, Manual of Remote Sensing, Vol. 2*, John Wiley & Sons, Inc., New York: New York, 1998.
- J.P. Hollinger, J.L. Pierce, and G.A. Poe, "SSM/I Instrument Evaluation," *IEEE Trans. Geosci. Remote Sensing*, Vol. 28, No. 5, pp. 781-790, Sept. 1990.
- J. Hollinger *et al.*, "Special Sensor Microwave/Imager User's Guide," Naval Research Laboratory, Washington, D.C., Dec. 14, 1987.
- J. Hollinger, "DMSP Special Sensor Microwave/Imager Calibration/Validation, Final Report, Volume 1," Naval Research Laboratory, Washington, D.C., July 1989.
- D. Hudson, J.R. Piepmeier, and D.G. Long, "Polarization Rotation Correction in Radiometry: An Error Analysis," *IEEE Transactions on Geoscience and Remote Sensing*, Vol. 45, No. 10, pp. 3212-3223, 2007.
- B.A. Ivanov, "Venusian impact craters on Magellan images: View from Venera 15/16," *Earth, Moon, and Planets*, 50/51, pp. 159-174, 1990.

- C.R. Jackson and J.R. Apel, eds., *Synthetic Aperture Radar Marine User's Manual*, U.S. Department of Commerce, ISBN 0-16-073214-X, Sept. 2004.
- T.J. Jackson and T.J. Schmugge, "Algorithm for the Passive Microwave Remote Sensing of Soil Moisture," in *Microwave Radiometry and Remote Sensing Applications* (P. Pampaloni, ed.), (Zeist), pp. 3-17, VSP, 1989.
- C.V. Jakowatz, D.E. Wahl, P.H. Eichel, D.C. Ghiglia, and P.A. Thompson, *Spotlight-Mode Synthetic Aperture Radar: A Signal Processing Approach*, Kluwer Academic Publishers, New York, NY, 1996.
- M.A. Janssen, ed., *Atmospheric Remote Sensing by Microwave Radiometry*, New York, NY: John Wiley, 1993.
- "Special Issue on Jason-1 Calibration/Validation," *Marine Geodesy*, Vol. 27, No. 1-2, 2004.
- J.W. Johnson, L.A. Williams, Jr., E.M. Bracalente, F.B. Beck, and W.L. Grantham, "Seasat-A satellite scatterometer instrument evaluation," *IEEE J. Oceanic Eng.*, Vol. OE-5, No. 2, pp. 138-144, 1980.
- R.L. Jordan, "The Seasat-A Synthetic Aperture Radar System," *IEEE J. Oceanic Eng.*, vol. OE-5, No. 2, pp. 154-163, 1980.
- R.L. Jordan, B.L. Huneycutt, M. Werner, "The SIR-C/X-SAR Synthetic Aperture Radar System," *Proceedings of the IEEE*, Vol. 79, No. 6, pp. 827-838, June 1991.
- W.L. Jones, R. Mehershahi, J. Zec, and D.G. Long, "SeaWinds on QuikScat radiometric measurements and calibration," *Proceedings IEEE Geoscience and Remote Sensing Symposium*, Honolulu, HI, pp. 1027-1027, 2000.
- A.S. Jones and T.H.V. Haar, "Passive Microwave Sensing of Cloud Liquid Water Over Land Regions," *Journal of Geophysical Research*, Vol. 95, pp. 16673-16683, September 1990.
- F. Karbou, "Two Microwave Land Emissivity Parameterizations Suitable for AMSU Observations," *IEEE Trans. Geosci. Remote Sensing*, Vol. 43, No. 8, pp. 1788-1795, Aug 2005.
- F. Karbou, C. Prigent, L. Eymard, and J.R. Pardo, "Microwave Land Emissivity Calculations Using AMSU Measurements," *IEEE Trans. Geosci. Remote Sensing*, Vol. 43, No. 5, pp. 948-959, May 2005.

- T. Kawanishi, T. Sezai, Y. Ito, K. Imaoka, T. Takeshima, Y. Ishido, A. Shibata, M. Miura, H. Inahata, and R.W. Spencer, "The Advanced Microwave Scanning Radiometer for the Earth Observing System (AMSR-E): NASDA's contribution to the EOS for global energy and water cycle studies," *IEEE Trans. Geosci. Remote Sensing*, Vol. 41, pp. 184-194, 2003.
- R.G. Kennett and F.K. Li, "Seasat Over-Land Scatterometer Data, Part I: Global Overview of the *Ku*-Band Backscatter Coefficients," *IEEE Transactions on Geoscience and Remote Sensing*, Vol. GE-27, No. 5, pp. 592-605, Sept. 1989.
- Y.H. Kerr, P. Waldteufel, J-P Wigneron, J. Martinuzzi, J. Font, and M. Berger, "Soil moisture retrieval from space: the Soil Moisture and Ocean Salinity (SMOS) mission," *IEEE Transactions on Geoscience and Remote Sensing*, Vol. 39, pp. 1729-1735, 2001.
- C. Kongoli, P. Pellegrino, R.R. Ferraro, N.C. Grody, and H. Meng, "A New Snowfall Detection Algorithm Over Land Using Measurements from the Advanced Microwave Sounding Unit (AMSU)," *Geophysical Research Letters*, Vol. 30, No. 14, pg. 1756. 2003.
- A. Kraszewski, ed., *Microwave Aquametry: Electromagnetic Wave Interaction with Water-Containing Materials*, Piscataway, NJ: IEEE Press, 1996
- G. Krieger, A. Moreira, H. Fiedler, I. Hajnsek, M. Werner, M. Younis, and M. Zink, "TanDEM-X: A Satellite Formation for High-Resolution SAR Interferometry," *IEEE Transactions on Geoscience and Remote Sensing*, Vol. 45, No. 11, pp. 3317-3341, Nov. 2007.
- G. Franschetti and R. Lanari, *Synthetic Aperture Radar Processing*, CRC Press, FL, 1999.
- P. Lecomte, A. Cavanie, and F. Gohin, "Recognition of Sea Ice Zones using ERS-1 Scatterometer Data," *Proceedings of IGARSS 93*, pp. 855-857, 1993.
- F.W. Leberl, *Radargrammetric Image Processing*, Norwood, MA: Artech House, Inc., 1990.
- T. Lee, J. Goerss, J. Hawkins, J. Turk, Z. Jelenak, P. Chang, "Windsat applications for weather forecasters and data assimilation," *IEEE Proc. International Geoscience and Remote Sensing Symposium*, pp. 4022-4025, 26-29 July 2005.
- B.G. Levi, "COBE Measures Anisotropy in Cosmic Microwave Background Radiation," *Physics Today*, pp. 17-20, June 1992.

- L. Li, E.G. Njoku, E. Im, P.S. Chang, and K. St. Germain, "A preliminary survey of radio-frequency interference over the U.S. in Aqua AMSR-E Data," *IEEE Trans. Geosci. Remote Sens.*, Vol. 42, No. 2, pp. 380-390, 2004.
- D.G. Long, M.R. Drinkwater, B. Holt, S. Saatchi, and C. Bertoia, "Global Ice and Land Climate Studies Using Scatterometer Image Data," *EOS, Transaction of the American Geophysical Union*, Vol. 82, No. 43, pg. 503, 23 Oct. 2001.
- D.G. Long and M.R. Drinkwater, "Azimuth Variation in Microwave Scatterometer and Radiometer Data over Antarctica," *IEEE Transactions on Geoscience and Remote Sensing*, Vol. 38, No. 4, pp. 1857-1870, 2000.
- D.G. Long and M.R. Drinkwater, "Cryosphere Applications of NSCAT Data," *IEEE Transactions Geoscience and Remote Sensing*, Vol. 37, No. 3, pp. 1671-1684, 1999.
- D.G. Long and G.B. Skouson, "Calibration of Spaceborne Scatterometers Using Tropical Rainforests," *IEEE Transactions on Geoscience and Remote Sensing*, Vol. 34, No. 2, pp. 413-424, Mar. 1996.
- D.G. Long and M.R. Drinkwater, "Greenland Observed at High Resolution by the Seasat-A Scatterometer," *Journal of Glaciology*, Vol. 32, No. 2, pp. 213-230, 1994.
- D. G. Long, C-Y Chi, and F. K. Li, "The Design of an Onboard Digital Doppler Processor for a Spaceborne Scatterometer," *IEEE Trans. Geosci. Remote Sensing*, Vol. 26, No. 6, pp. 869-878, Nov. 1988.
- J.L. MacArthur, P.C. Marth, Jr., and J.G. Wall, "The Geosat radar altimeter," *Johns Hopkins APL Technical Digest*, Vol. 8, No. 2, pp. 176-181, 1971
- S.N. Madsen, H.A. Zebker, and J. Martin, "Topographic mapping using radar interferometry: Processing techniques", *IEEE Transactions on Geoscience and Remote Sensing*, vol. 31, pp. 246-256, January 1993.
- C.F. Martin and R. Kolenkiewicz, "Calibration validation for the GEOS-3 altimeter," *J. Geophys. Res.*, Vol. 86, pp. 6369-6381, 1981.
- T.V. Martin, H.J. Zwally, A.C. Brenner, and R.A. Bindshadler, "Analysis and re-tracking of continental ice sheet radar altimeter waveforms," *Journal of Geophysical Research* Vol. 88, No. C3, 1608-16, 1983.
- M.J. McFarland, R.L. Miller, and C.M.U. Neale, "Land Surface Temperature Derived From the SSM/I Passive Microwave Brightness Temperatures," *IEEE Trans. Geosci. Remote Sensing*, Vol. 28, pp. 839-845, September 1990.

- K. Maeda, M. Notomo, S. Ogawa, H. Sato, "Verification Results of Mos-1 Microwave Scanning Radiometer (msr)," *IEEE Proc. International Geoscience and Remote Sensing Symposium*, pp. 978-981, 10-14 Jul. 1989.
- R. Meneghini, T. Iguchi, T. Kozu, L. Liao, K. Okamoto, J.A. Jones and J. Kwiatkowski, "Use of the surface reference technique for path attenuation estimates from the TRMM precipitation radar," *J. Appl. Meteor.*, Vol. 39, pp. 2053-2070, 2000.
- R. Meneghini and T. Kozu, *Spaceborne Weather Radar*, Norwood, MA, Artech House, 1990.
- T. Misra, A.M. Jha, D. Putrevu, J. Rao, D.B. Dave, and S.S. Rana, "Ground calibration of multifrequency scanning microwave radiometer (MSMR)," *IEEE Transactions on Geoscience and Remote Sensing*, Vol. 40, pp. 504-508, 2002.
- J. Moreira, M. Schwabisch, G. Fornaro, R. Lanari, R. Bamler, D. Just, U. Steinbrecher, H. Breit, M. Eineder, G. Granceschetti, D. Geudtner, and H. Rinkel, "X-SAR interferometry: First results," *IEEE Transactions on Geoscience and Remote Sensing*, Vol. 33, No. 4, pp. 950-956, 1995.
- F. Naderi, M.H. Freilich, and D.G. Long, "Spaceborne Radar Measurement of Wind Velocity Over the Ocean—An Overview of the NSCAT Scatterometer System," *Proceedings of the IEEE*, pp. 850-866, Vol. 79, No. 6, June 1991.
- NASA Aquarius web site <http://aquarius.gsfc.nasa.gov/>, 2007.
- Y. Nemoto, et al., "Japanese Earth Resources Satellite-1 Synthetic Aperture Radar," *Proceedings of the IEEE*, Vol. 79, No. 6, pp. 800-809, June 1991.
- E.G. Njoku, J.M. Stacey, and F.T. Barath, "The Seasat Scanning Multichannel Microwave Radiometer: Instrument Design and Performance," *IEEE J. Oceanic Eng.*, Vol. OE-5, No. 2, pp. 100-115, 1980.
- E.G. Njoku and D. Entekhabi, "Passive Microwave Remote Sensing of Soil Moisture," *J. Hydrology*, Vol. 184, pp. 101-129, 1996.
- E. Njoku, W. Wilson, S. Yueh, and Y. Rahmat-Samii, "A Large-Antenna Microwave Radiometer-Scatterometer Concept for Ocean Salinity and Soil Moisture Sensing," *IEEE Transactions on Geoscience and Remote Sensing*, November, 2000.
- E. Njoku, M. Spencer, K. McDonald, J. Smith, P. Houser, T. Doiron, P. O'Neill, R. Girard, D. Entekhabi, "The HYDROS Mission: Requirements and System

- Design,” *Proceedings of the 2004 IEEE Aerospace Conference*, Big Sky, MT, March 7-12, 2003.
- E.G. Njoku, P. Ashcroft, T.K. Chan and L. Li, “Global Survey and Statistics of Radio-Frequency Interference in AMSR-E Land Observations,” *IEEE Transactions on Geoscience and Remote Sensing*, v. 43, no. 5, pp. 938-947, May, 2005.
- C. Oliver and S. Quegan, *Understanding Synthetic Aperture Radar Images*, Norwood, MA: Artech House, Inc. 1990.
- P. Pampaloni and S. Paloscia, “Microwave Emission and Plant Water Content: A Comparison Between Field Measurement and Theory,” *IEEE Trans. Geosci. Remote Sensing*, Vol. 24, pp. 900-904, November 1986.
- G.H. Pettengill, P.G. Ford, W.T.K. Johnson, R.K. Raney, and L.A. Soderblom, “Magellan: Radar Performance and Data Products,” *Science*, Vol. 252, pp. 260-265, 1991.
- G.H. Pettengill, “Radar Astronomy”, in M.I. Skolnik (ed.), *Radar Handbook*, New York, NY: McGraw-Hill, 1970.
- J. Piepmeier, E.G. Njoku, and D.G. Long “Stokes Antenna Temperatures,” *IEEE Transactions on Geoscience and Remote Sensing*, 2007.
- J.J. Plaut and R.E. Arvidson, “Comparison of Goldstone and Magellan radar data in the equatorial plains of Venus,” *Journal of Geophysical Research*, Vol. 97, No. E10, pp. 16279-16291, 1992.
- M.D. Goldberg and F. Weng ”Advanced Technology Microwave Sounder,” pp. 243-253, in J.J. Qu, W. Gao, M. Kafatos, R.E. Murphy and V.V. Salomonson, eds., *Earth Science Satellite Remote Sensing Vol. 1: Science and Instruments*, Springer, Berlin, 2006.
- Q.P. Remund and D.G. Long, “Sea Ice Extent Mapping Using Ku band Scatterometer Data,” *Journal of Geophysical Research*, Vol. 104, No. C5, pp. 11515-11527, 1999.
- A. Reigber and R. Scheiber, “Airborne differential SAR interferometry: first results at L-band”, *IEEE Transactions on Geoscience and Remote Sensing*, vol. 41, pp. 1516-1520, June 2003.
- E. Rodriguez and J.M. Martin, “Theory and design of interferometric synthetic aperture radars,” *IEEE Proc. of Radar and Signal Processing*, Vol. 139, No. 2, pp. 147-159, 1992.

- M. Rokey, "Magellan Special Radar Flight Experiments," *Journal of Spacecraft and Rockets*, Vol. 30, No. 6, 1993.
- C.S. Ruf, C.T. Swift, A.B. Tanner, and D.M. LeVine, "Interferometric Synthetic Aperture Radiometry for the Remote Sensing of the Earth," *IEEE Transactions on Geoscience and Remote Sensing*, Vol. 26, No. 5, pp. 597-611, 1988.
- C. Ruf, S. Keihm, B. Subramanya, and M. Janssen, "TOPEX/POSEIDON Microwave Radiometer (TMR): I. Instrument Description and Antenna Calibration," *IEEE Transactions on Geoscience and Remote Sensing*, Vol. 33, No. 1, pp. 125-137, Jan. 1995.
- K. Rohlfs and T.L. Wilson, *Tools of Radio Astronomy*, Springer-Verlag, Berlin, Germany, 1996.
- A. Rosenqvist, M. Shimada, N. Ito, and M. Watanabe, "ALOS PALSAR: A Pathfinder Mission for Global-Scale Monitoring of the Environment," *IEEE Transactions on Geoscience and Remote Sensing*, Vol. 45, No. 11, pp. 3307-3316, Nov. 2007.
- D.T. Sandwell, "Geophysical Applications of Satellite Altimetry," *Reviews of Geophysics Supplement*, p. 132-137, 1990.
- R.S. Saunders, A.J. Spear, P.C. Allin, R.S. Austin, A.L. Berman, R.C. Chandlee, J. Clark, A.V. DeCharon, E.M. DeJong, D.G. Griffith, J.M. Gunn, S. Hensley, W.T.K. Johnson, C.E. Kirby, K.S. Leung, D.T. Lyons, G.A. Michaels, J. Miller, R.B. Morris, A.D. Morrison, R.G. Piereson, J.F. Scott, S.J. Shaffer, J.P. Slonski, E.R. Stofan, T.W. Thompson, and S.D. Wall, "Magellan mission overview," *J. Geophys. Res.*, Vol. 97, No. E8, pp. 13067-13090, 1992.
- R.S. Saunders, G.H. Pettengill, R.E. Arvidson, B. Sjogren, W.T.K. Johnson, L.J. Pieri, "The Magellan Venus radar mapping mission," *J. Geophys. Res.*, Vol. 95, No. B6, pp. 8339-8355, 1990.
- M. Shimada, "SAR programmes in JAXA: from JERS-1 to the future," *IEE Proc. Radar, Sonar and Navigation*, Vol. 153, No. 2, pp. 122-128, 2006.
- N. Skou and D. Le Vine, *Microwave Radiometer Systems: Design and Analysis*, Artech House, Boston, 2006.
- C. Smoot, C. Bennett, R. Weber, et al., "COBE Differential Microwave Radiometers: Instrument Design and Implementation," *The Astronomical Journal*, Vol. 360, pp. 685-695, Sept. 1990.

- M.W. Spencer, C. Wu, and D.G. Long, "Improved Resolution Backscatter Measurements with the SeaWinds Pencil-Beam Scatterometer," *IEEE Transactions on Geoscience and Remote Sensing*, Vol. 38, No. 1, pp.89-104, 2000.
- M.W. Spencer, W-Y Tsai, and D.G. Long, "High Resolution Measurements with a Spaceborne Pencil-Beam Scatterometer Using Combined Range/Doppler Discrimination Techniques," *IEEE Transactions on Geoscience and Remote Sensing*, Vol. 41, No. 3, pp. 567-581, 2003.
- D.N. Spergel, et al., "First-year Wilkinson Microwave Anisotropy Probe (WMAP) observations: Determination of cosmological parameters," *Astrophys. J. Suppl. Ser.*, Vol. 148, No. 1, pp. 175-194, Sept. 2003.
- M. Stangl, R. Werninghauw, B. Schweizer, C. Fischer, M. Brandfass, J. Mittermayer, and H. Breit, "TerraSAR-X Technologies and First Results," *Proc. Inst. Electr. Eng. – Radar, Sonar Navig.*, Vol. 153, No. 2 pp. 86-95, Apr. 2006.
- H. Stephen and D.G. Long, "Microwave Backscatter Modeling of Erg Surfaces in the Sahara Desert," *IEEE Transactions on Geoscience and Remote Sensing*, Vol. 43, No. 2, pp. 238-247, 2005.
- H. Stephen and D.G. Long, "Modeling Microwave Emissions of Erg Surfaces in the Sahara Desert," *IEEE Transactions on Geoscience and Remote Sensing*, Vol. 43, No. 12, pp. 2822-2830, 2005.
- G.L. Stephens, et al., "The Cloudsat Mission and the A-Train," *BAMS*, pp. 1770-1790, Dec. 2002.
- E.R. Stofan, D.L. Evans, C. Schmullius, B. Holt, J.J. Plaut, J. von Zyl, S.D. Wall, J. Way, "Overview of Results of Spaceborne Imaging Radar-C, X-Band Synthetic Aperture Radar (SIR-C/X-SAR)," *IEEE Transactions on Geoscience and Remote Sensing*, Vol. 33, No. 4, pp. 817-828, July 1995.
- A. Stogryn, "Estimates of Brightness Temperatures from Scanning Radiometer Data," *IEEE Trans. Antennas Propagat.*, v. AP-26, no. 5, pp 720-726, Sept. 1978.
- I.A. Strukov, A.A. Brukhanov, D.P. Skulachev and M.V. Sazhin, "The Relikt-1 experiment - New results," *Monthly Notices of the Royal Astronomical Society*, Vol. 258, No. 2, pp 37-40, 15 Sept. 1992.
- S. Takeuchi, Y. Nakayama, and T. Tomita, "Integration of SST Data Set Using MOS-1 Satellite Data for Validation of SST Retrieval," *IEEE Proc. International Geoscience and Remote Sensing Symposium*, pp. 149-151, 1993.

- R.H. Thomas, R.A. Bindshadler, R.L. Cameron, F.D. Carsey, B.Holt, T.J. Hughes, C.W.M. Swithinbank, I.M. Whillans, and H.J. Zwally, "Satellite Remote Sensing for Ice Sheet Research," *NASA Technical Memorandum*, 86233, 27, 1985.
- W.F. Townsend, "An Initial assessment of the performance achieved by the Seasat-1 radar altimeter," *IEEE J. Oceanic Engineering*, Vol. OE-5, pp. 80-92, 1980.
- L. Tsang, J.A. Kong, and R.T. Shin, *Theory of Microwave Remote Sensing*, New York: Wiley, 1985.
- W-Y Tsai, J.E. Graf, C. Winn, J.N. Huddleston, S. Dunbar, M.H. Freilich, F.J. Wentz, D.G. Long, and W.L. Jones, "Postlaunch Sensor Verification and Calibration of the NASA Scatterometer," *IEEE Transactions on Geoscience and Remote Sensing*, Vol. 37, No. 3, pp. 1517-1542, 1999.
- F.T. Ulaby, R.K. Moore, and A.K. Fung, *Microwave Remote Sensing – Active and Passive*, Vols. 1 and 2, Addison-Wesley Publishing Co., Reading, Mass., 1981.
- F.T. Ulaby and C. Elachi, eds., *Radar Polarimetry for Geoscience Applications*, Norwood, MA: Artech House, Inc., 1990.
- G.L. Verschuur, *The Invisible Universe Revealed*, Springer-Verlag, New York, New York, 1987.
- N.K. Vyas and M.K. Dash, "Oceansat - MSMR Observers interesting features on the frozen continent and surrounding sea," *Journal of Indian Society of Remote Sensing*, Vol. 28, pg. 67, 2000.
- N.K. Vyas, S.M. Bhandari, M.K. Dash, N.K. Vyas, P.C. Pandey, N. Khare, A. Khanolkar, N. Sharma, *An Atlas of Antarctic Sea Ice from OCEANSAT-1 MSMR (June 1999-September 2001)*, National Centre for Antarctic and Ocean Research, Goa - India, 2004.
- H. Wakabayashi, N. Ito, and T. Hamazaki, "PALSAR System on the ALOS," in, H. Fujisada (ed), "Sensors, Systems, and Next-Generation Satellites II," *Proc. SPIE Vol. 3498*, pp. 181-189, 1998.
- F.J. Wentz, "Measurement of oceanic wind vector using satellite microwave radiometers," *IEEE Transactions on Geoscience and Remote Sensing*, Vol. 30, No. 5, pp. 960-972, 1992.
- F.J. Wentz, User's Manual SSM/I Antenna Temperature Tapes, Remote Sensing Systems (<http://www.ssmi.com/>), Santa Rosa, CA, 1991.

- NOAA NPOESS WindSat Website <http://www.ipo.noaa.gov/Projects/windsat.html>, 2007.
- V.R. Wismann, K. Boehnke, and C. Schmullius, "Monitoring Ecological Dynamics in Africa with the ERS-1 Scatterometer," *Proceedings of the International Geoscience and Remote Sensing Symposium*, pgs. 1523-1525, 1995.
- R. Wohlleben, H. Mattes, T.H. Krichbaum, *Interferometry in Radioastronomy and Radar Techniques*, Kluwer Academic Publishers, Dordrecht, The Netherlands, 1991.
- I.H. Woodhouse, *Introduction to Microwave Remote Sensing*, CRC Press, Boca Raton, Florida, 2006.
- J.D. Young, "Active Microwave Measurement of Sea-surface Winds from Space," Ph.D. Dissertation, Kansas University, 1976.
- S.H. Yueh, R. Kwok, F.K. Li, S.V. Nghiem, W.J. Wilson, and J.A. Kong, "Polarimetric Passive Remote Sensing of Ocean Wind Vector," *Radio Science*, Vol. 28, pp. 799-814, 1994.
- H.A. Zebker and R. M. Goldstein, "Topographic mapping from interferometric synthetic aperture radar observations," *J. Geophys. Res.*, vol. 91, no. B5, pp. 4993-4999, 1986.
- J. Zec, W.L. Jones, and D.G. Long, "NSCAT Normalized Radar Backscattering Coefficient Biases Using Homogenous Land Targets," *Journal of Geophysical Research*, Vol. 104, No. C5, pp. 11557-11568, 1999.
- H.J. Zwally, R.A. Bindschadler, A.C. Brenner, T.V. Martin, R.H. Thomas, "Surface elevation contours of Greenland and Antarctic ice sheets," *Journal of Geophysical Research* Vol. 88, No. C3, pp. 1589-1596, 1983.